

מכון ויצמן למדע

WEIZMANN INSTITUTE OF SCIENCE



## The proteasome regulator PSME4 modulates proteasome activity and antigen diversity to abrogate antitumor immunity in NSCLC

### Document Version:

Accepted author manuscript (peer-reviewed)

### Citation for published version:

Javitt, A, Shmueli, MD, Kramer, MP, Kolodziejczyk, AA, Cohen, IJ, Radomir, L, Sheban, D, Kamer, I, Litchfield, K, Bab-Dinitz, E, Zadok, O, Neiens, V, Ulman, A, Wolf-Levy, H, Eisenberg-Lerner, A, Kacen, A, Alon, M, Rêgo, AT, Stacher-Priehse, E, Lindner, M, Koch, I, Bar, J, Swanton, C, Samuels, Y, Levin, Y, da Fonseca, PCA, Elinav, E, Friedman, N, Meiners, S & Merbl, Y 2023, 'The proteasome regulator PSME4 modulates proteasome activity and antigen diversity to abrogate antitumor immunity in NSCLC', *Nature Cancer*, vol. 4, no. 5, pp. 629-647. <https://doi.org/10.1038/s43018-023-00557-4>

Total number of authors:

30

### Digital Object Identifier (DOI):

[10.1038/s43018-023-00557-4](https://doi.org/10.1038/s43018-023-00557-4)

### Published In:

Nature Cancer

### License:

CC BY

### General rights

@ 2020 This manuscript version is made available under the above license via The Weizmann Institute of Science Open Access Collection is retained by the author(s) and / or other copyright owners and it is a condition of accessing these publications that users recognize and abide by the legal requirements associated with these rights.

### How does open access to this work benefit you?

Let us know @ [library@weizmann.ac.il](mailto:library@weizmann.ac.il)

### Take down policy

The Weizmann Institute of Science has made every reasonable effort to ensure that Weizmann Institute of Science content complies with copyright restrictions. If you believe that the public display of this file breaches copyright please contact [library@weizmann.ac.il](mailto:library@weizmann.ac.il) providing details, and we will remove access to the work immediately and investigate your claim.

## Altered proteasome composition attenuates tumor immunogenicity in NSCLC

Aaron Javitt<sup>\*1</sup>, Merav D. Shmueli<sup>\*1</sup>, Matthias P Kramer<sup>1</sup>, Ivan Cohen<sup>1</sup>, Iris Kamer<sup>2</sup>, Elizabeta Bab-Dinitz<sup>2</sup>, Oranit Zadok<sup>2</sup>, Jair Bar<sup>2</sup>, Vanessa Welk<sup>3</sup>, Mercedes Rosenwald<sup>1</sup>, Adi Ulman<sup>1</sup>, Solaiman Masarwi<sup>1</sup>, Hila Levy Wolf<sup>1</sup>, Avital Lerner-Eisenberg<sup>1</sup>, Assaf Kacen<sup>1</sup>, Osnat Bartok<sup>4</sup>, Paula De Fonseca<sup>5</sup>, Elvira Stacher-Priehse<sup>6</sup>, Michael Lindner<sup>6</sup>, Ina Koch<sup>6</sup>, Yardena Samuels<sup>4</sup>, Nir Friedman<sup>1</sup>, Yishai Levin<sup>7</sup>, Silke Meiners<sup>3</sup>, Yifat Merbl<sup>\$1</sup>

\*Equal contribution

\$ Corresponding author: Yifat.merbl@weizmann.ac.il

<sup>1</sup>Department of Immunology, Weizmann Institute of Science, Rehovot, Israel.

<sup>2</sup>Thoracic Unit, Cancer center, Sheba Medical Center, Israel.

<sup>3</sup>Comprehensive Pneumology Center (CPC), University Hospital, Ludwig-Maximilians University, Helmholtz Zentrum Muenchen, Munich, Member of the German Center for Lung Research (DZL), Germany

<sup>4</sup>Department of Molecular and Cell Biology, Weizmann Institute of Science, Rehovot, Israel.

<sup>5</sup>Structural Biology, University of Glasgow, UK.

<sup>6</sup> Asklepios Lung Clinic Munich-Gauting, 82131, Gauting, Germany

<sup>7</sup>INCPM, Weizmann Institute of Science, Israel.

## Abstract

Immunoproteasomes are key for antigen processing and presentation and have been recently implicated in the responsiveness to immunotherapy. By profiling the degradation landscape in lung cancer tissue and adjacent controls we found tumor-specific alterations and increased proteasomal degradation in non-small cell lung cancer (NSCLC). Our analysis revealed that the proteasome activator, PA200/PSME4, is increased in NSCLC and is associated with poor survival. We show that PSME4 reduces tumor inflammation by inhibiting interferon signaling and the downstream activation of its transcriptional program. Further, we found that PSME4 directly binds to and attenuates the activity of the immunoproteasome, which in turn restricts the HLA landscape. We therefore hypothesized that these cancer-associated proteasomes may contribute to resistance mechanisms to immunotherapy. Consistent with this possibility, we found that the ratio between PSME4 and the immunoproteasome was significantly associated with poor response to immune checkpoint blockade. Finally, we could show that reducing PSME4 expression drives anti-tumor immunity and inhibits tumor growth *in vivo*. Collectively, our results provide novel understanding for regulatory mechanisms underlying tumor proteostasis and offer PSME4 as a novel target for sensitizing response to immunotherapy in NSCLC and other cancer types.

## Introduction

Recent advances in cancer immunotherapy have revolutionized clinical care of cancer patients in several cancer types, including lung cancer. While immune checkpoint inhibitors (ICI) show great promise, many tumors are resistant to these therapies and major efforts are underway to reveal the underlying mechanisms (1–4). Mutational burden, inflammation and immune infiltration were all suggested to play critical roles in response to ICI in melanoma and Non-Small Cell lung Cancer (NSCLC; ((5–12)). High levels of immunoproteasomes, which are associated with improved antigen presentation on MHC class I, were also shown to be predictors of response to ICI in melanoma (8, 10, 13–16). Yet, whether this association will hold true in other types of cancers, such as NSCLC, is unknown.

The proteasome is the key intracellular protease involved in the generation of MHC class I antigens (17). Specifically, immunoproteasome function has been shown crucial for the generation of tumor-associated antigens that drive effective cytotoxic clearing of tumor cells by CD8<sup>+</sup> T cells (18–23). The core of the immuno- and constitutive 20S proteasome differs by three catalytic subunits, i.e. PSMB8, PSMB9, PSMB10 that are encoding LMP7, LMP2 and MECL1, respectively. The immunoproteasome is induced by inflammatory cytokines, such as interferons (IFN) and is constitutively expressed mainly in immune cells (24–26). Previous studies uncovered an altered cleavage pattern by the immunoproteasome, which is responsible for generating more hydrophobic peptides, that are thought to be preferential for MHC class I presentation. Beyond antigenicity, immunoproteasomes were also shown to mediate inflammatory signaling and innate and adaptive immune cell activation (27, 28). Recent clinical development of proteasome and immunoproteasome inhibitors further highlights the importance of elucidating their role in the context of anti-tumor immunity. Aside from changes in the catalytic sites, proteasome function is also affected by specific regulatory particles such as the 19S subunit (PSMC1-6 and PSMD1-14), and the alternative regulators PA28 $\alpha\beta$  (PSME1+2), PA28 $\gamma$  (PSME3) or PA200 (PSME4) (29–32) that bind the catalytic core. The 19S has been shown to be pivotal for binding of ubiquitinated species and substrate unfolding, while the others are suggested to have more specialized roles, including mediating inflammatory responses, histone degradation, and the response to DNA damage (29, 31, 33–40). The different catalytic cores, together with the diverse range of regulatory subunits, introduce great potential diversity for generating hybrid proteasomes of the 20S core particle with different combinations of regulatory caps, thereby altering protein cleavage (41–45). Yet, the physiological role of such hybrid forms in general and how they may shape the cellular degradation landscape in cancer (43) remains poorly understood.

It has been suggested that the binding of alternative regulators to the 20S core particle mediates specific substrate degradation (30). We have recently developed a novel approach to profile the degradation landscapes in cells and tissues using MS analysis of proteasome-cleaved peptides (MAPP) (46, 47). Here, we applied this method to analyze clinical samples of resected lung tumors. We discovered a distinct signature of proteasome degradation that was

associated with NSCLC. Importantly, we found an altered proteasome composition and increased degradation of proteins in the cancerous tissues when compared to adjacent non-tumor tissue. Notably, we found significant upregulation of PSME4, and could show it is associated with poor survival of patients with NSCLC. Biochemical and cellular characterization of the functional consequences of PSME4 upregulation revealed that it directly attenuates immunoproteasome activity leading to reduced tumor immunogenicity. Further, we show that PSME4-associated proteasomes play an anti-inflammatory role in NSCLC, contributing to tumor growth *in vivo*. Finally, we demonstrate that PSME4 is associated with a ‘cold’ tumor signature which may impact resistance to ICI therapy. Collectively, our findings uncover the degradation landscape of NSCLC and elucidate a causal role of PSME4 in shaping the tumor landscape to suppress anti-tumor immunity. Beyond novel insight into proteasome biology, our work introduces a novel paradigm by which proteasome hybrids and composition should be examined in the context of tumor immunogenicity and immunotherapy in NSCLC and beyond.

## Results

To analyze the degradation landscape in NSCLC we performed mass spectrometry analysis of proteolytic peptides (MAPP; (46)) on tumor and adjacent lung tissues (Fig. 1A, Table S1). This analysis allows us to capture proteins as they are targeted for proteasomal degradation (47). We found significantly more proteasome-cleaved peptides in the tumor degradome as compared to the adjacent tissue (Fig. 1B and S1A). Both protein abundance, determined through whole cell proteomics, and MAPP degradation analyses effectively separated cancerous tissue from adjacent lung tissue (Fig. 1C and S1B to E and Table S2 and S3). Focusing on the degradation signature, we identified 59 differential proteins which were degraded mostly in the tumor samples and were shared among patients (Fig. 1D and S2A to B, Table S4). We could further confirm mRNA expression of most of these targets based on the TCGA lung cancer cohort (Fig. S2C; (48)). Notably, these cancer-specific degradation substrates were not among the most differential in protein abundance and about 10%, were not detected in the whole cell proteomic at all (Fig. S2B to C). This suggests that the degradation signature identified by MAPP reflects proteome changes that may not be captured by whole cell proteomics. Examination of the nature of the differential degradation substrates revealed proteins from a diverse set of biological functions and a significant enrichment for nuclear proteins, which were preferentially degraded in the tumor samples (Fig. 1E-F). By contrast, no significant change was observed in the degradation of cytosolic proteins (Fig 1G). The increased number of proteasome-cleaved peptides, together with the observed increase in nuclear degradation, which was previously associated with specific regulatory subunits (34, 38, 49), suggests that proteasome composition may be altered between the tumor and adjacent tissue. Comparing the abundance of proteasome subunits in the cancer and adjacent control tissue in whole cell proteomics, we found that the regulatory caps (PSME1, PSME2, PSME3 and PSME4) were increased in expression in the cancerous tissue, whereas no significant changes were observed in the core subunits of the constitutive 20S and

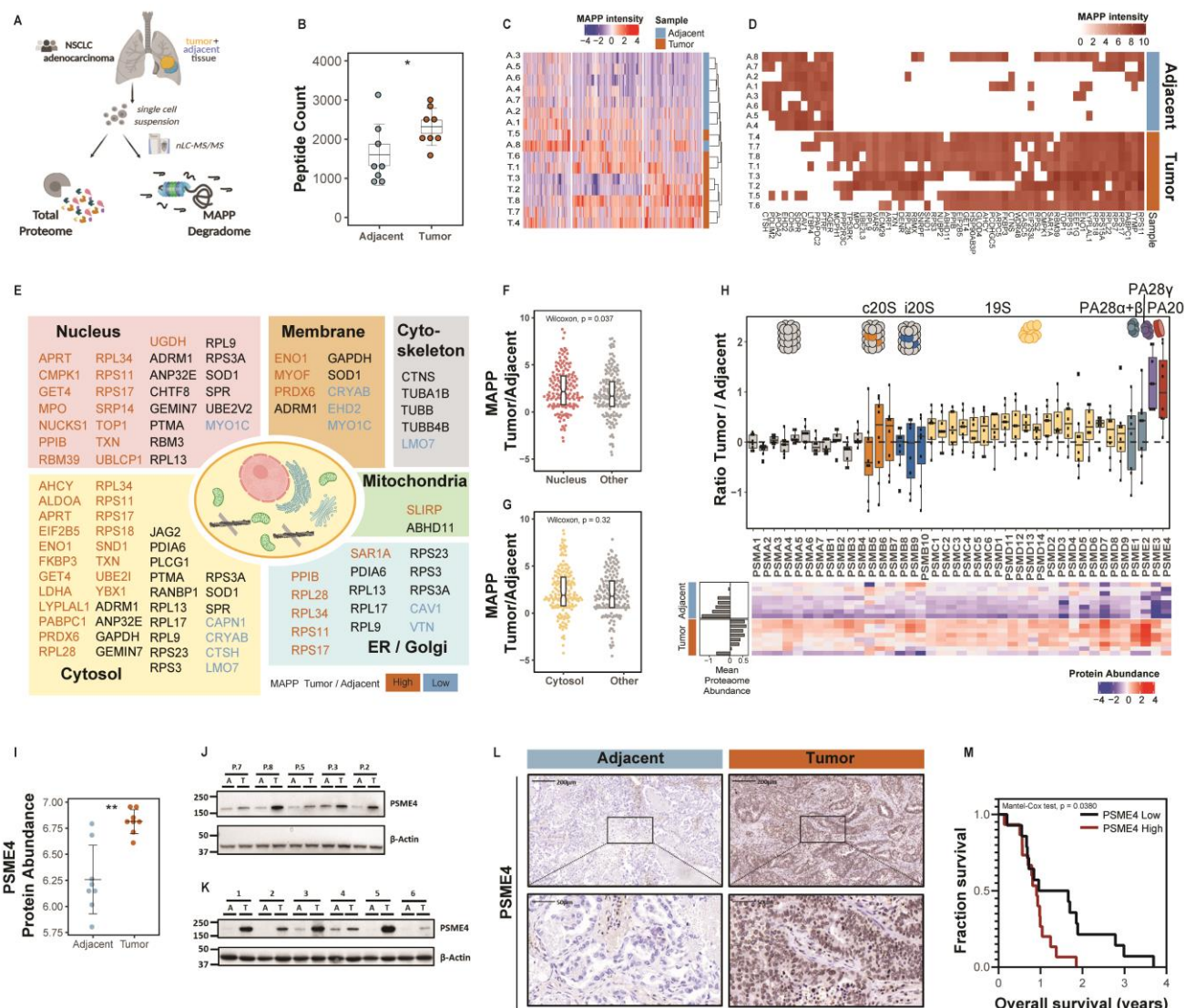


**Fig 1. Increased PSME4 levels alter proteasome composition and reduce survival in NSCLC.** (A) Schematic representation of the workflow. Analysis of lung adenocarcinoma tumor and adjacent lung tissue was performed using standard whole cell extract proteomics to assess protein abundance and MAPP to study the proteasome composition and degradome of the sample (N=16 samples). (B) The number of peptides identified in the tumor degradome (MAPP) was significantly higher than the adjacent samples (Wilcoxon paired t test  $p = 0.016$ ). (C) Heatmap of the peptides ( $n = 4891$ ) identified in the tumor and adjacent degradomes by MAPP. Rows and columns were clustered using spearman clustering distance and rows split by kmeans (clusters = 3). (D) Proteins identified as degraded primarily in tumors or adjacent tissue ( $n = 59$ ). Rows and columns were clustered using semi-supervised Pearson distances. (E) Proteins identified in MAPP organized by their annotated location (Human Protein Atlas). Proteins are colored based on the mean of degradation ratios between tumor and adjacent tissues across patients (orange: above median degradation ratio, blue: negative ratio, black: intermediate). Proteins which are annotated to more than one organelle appear twice. (F-G) The mean ratio of degradation (MAPP) between the tumor and adjacent tissues for proteins annotated to the nucleus (F) or cytosol (G) versus other proteins. The nuclear proteins on average had significantly higher ratio compared to the background proteins (Wilcoxon  $p = 0.037$ ). (H) The abundance of all the proteasome subunits based on the whole cell (WC) Proteomics across the samples (Log 10 Normalized LFQ Abundance, bottom of the figure). Normalized mean abundance of the proteasome subunits in the sample is shown on the right. The ratio between subunit abundance in the proteasome immunoprecipitation from tumor and adjacent tissue per patient (top). Colors and diagrams indicate the identity of the proteasome subunits. (I) PSME4 is significantly more abundant in the pulldown from tumor samples as compared to adjacent tissue (\*\*Wilcoxon  $P = 0.0078$ ). (J-K) Tumor and adjacent tissue from an Israeli (J) or German (K) cohort was blotted for PSME4 abundance with tumors showing higher total PSME4 levels.  $\beta$ -Actin was blotted as a loading control. (L) Immunohistochemistry of PSME4 in the tumor and adjacent tissues shows increased abundance in the tumor tissue with nuclear localization in both. (M) Lung cancer samples showed that tumors with increased staining of PSME4 (immunohistochemistry) had significantly reduced survival compared to patients with tumors expressing low levels of PSME4.

immunoproteasome (Fig. 1H). Among these, the nuclear proteasome subunits PSME3 (encoding PA28 $\gamma$ ) and PSME4 (encoding PA200) were the most upregulated (Fig. 1H-I and S3A). This observation was confirmed in our MAPP analysis revealing a similar enrichment of these regulators in cancer tissue (Fig 1H upper panel). Previous studies described an association between beneficial prognosis in NSCLC and high expression of PSME1 and PSME2 (encoding PA28 $\alpha\beta$ ), while targeting of PSME3 was shown to inhibit NSCLC tumor growth (43, 50). However, a role for PSME4 in tumors has not been examined to date and therefore we chose to focus on it.

We found that PSME4 is abundantly expressed in NSCLC tumors compared to adjacent lung tissue as demonstrated in two independent patient cohorts (Fig. 1J and K and S3B to C). Immunohistochemical staining confirmed increased PSME4 abundance mainly in the nucleus of NSCLC lung cancers (Fig 1L and S3D and E). To further substantiate the relevance of PSME4 in clinical settings, we stained lung tumor samples of patients with NSCLC lung adenoma carcinoma (LUAD), squamous cell lung cancer (SQCLC) or small cell lung cancer (SCLC) (n=60) for PSME4 protein expression. Of note, high levels of PSME4 were specifically detected in LUAD and SQCLC compared to SCLC and correlated with poor prognosis as indicated by a significant decrease in patient survival (Fig. 1M and S3F). PSME4 is associated with DNA repair (33, 34, 36, 38, 39), and its deficiency increased sensitivity to ionizing radiation in cancer (35). Furthermore, smoking is associated with alterations in proteasome activity (51). We therefore speculated that PSME4 expression was upregulated by smoking-induced DNA damage. Indeed, analysis of NSCLC expression data (TCGA LUAD (48)) revealed higher PSME4 expression in patients with a history of smoking, in correlation with increased tumor mutational burden and DNA repair signatures (52) (Fig. S4A to C).

The high expression of PSME4 in NSCLC suggests that this proteasome regulator shapes the degradation landscape of tumor cells through modulation of proteasome activity. Proteolytic activity of the proteasome differs between constitutive 20S and immunoproteasome (24–26, 53). We assessed proteasome activity in cellular extracts of A549 lung cancer cells upon addition of purified PSME4 using model substrates for defined constitutive and immunoproteasome cleavage sites (54)(Fig. S5). We confirmed that the recombinant PSME4 effectively bound to 20S and 26S proteasome complexes in functional extracts (Fig. S6A and B). We observed an increase in the caspase-like ( $\beta$ 1) and a decrease in the tryptic-like ( $\beta$ 2) and chymotryptic-like ( $\beta$ 5) activity of the constitutive proteasome upon addition of recombinant PSME4 (Fig. 2A-C). Intriguingly, PSME4 inhibited both the  $\beta$ 1i and  $\beta$ 5i activities under inflammatory conditions (stimulated with TNF $\alpha$  and IFN $\gamma$ ), in which the immunoproteasome is predominant (Fig. 2D and E). However, under steady state-conditions a slight increase in the  $\beta$ 5i chymotryptic-like activity is observed (Fig. 2E). These results suggest that PSME4 differentially regulates the catalytic activities of the proteasome. This PSME4-mediated shift in proteolytic activities possibly counteracts the generation of antigenic epitopes by the immunoproteasome under inflammatory conditions. Immunoprecipitation of PSME4 and biochemical fractionation confirmed that it interacts with the constitutive and immunoproteasome core subunits as

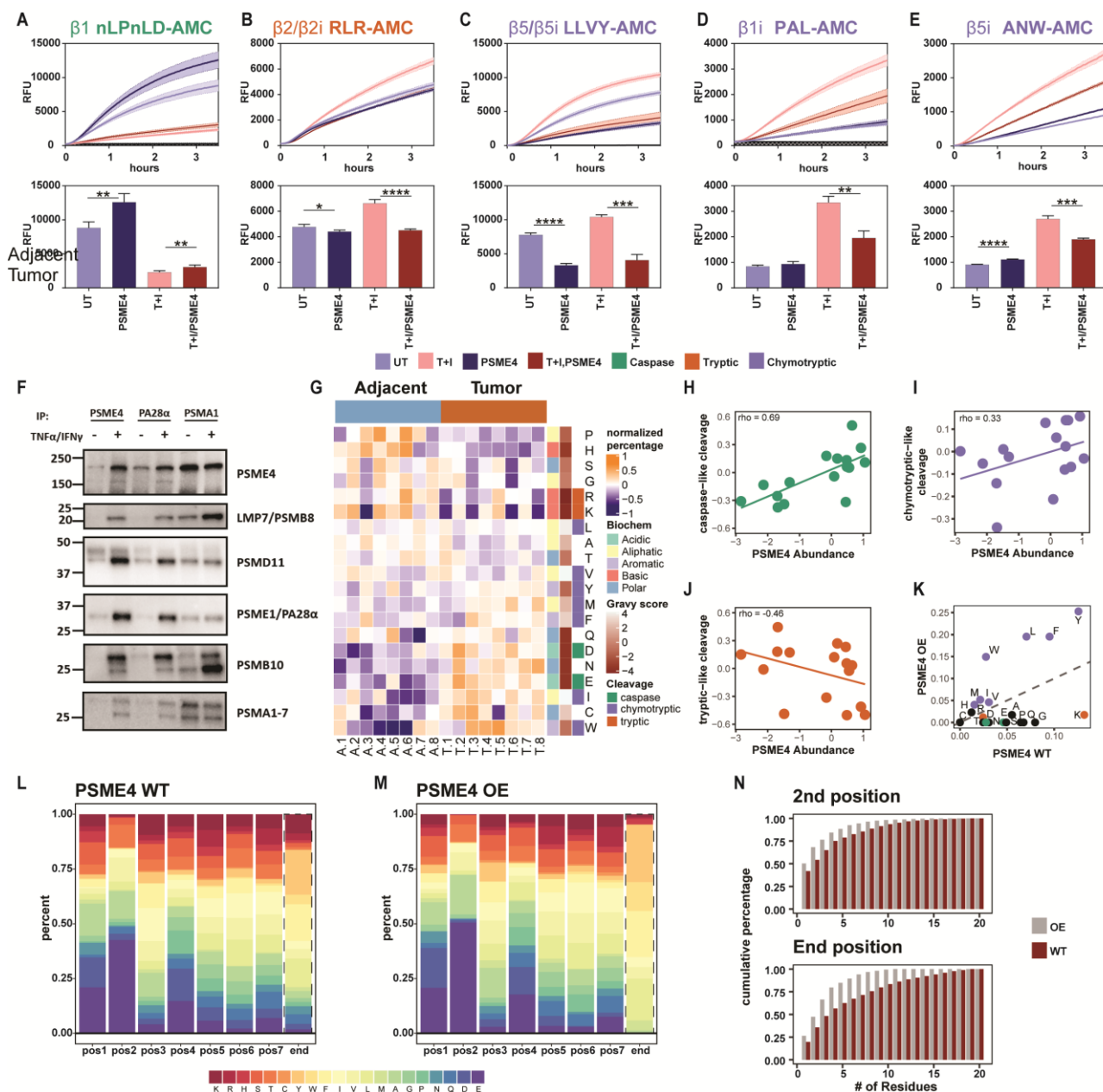


**Fig 2. PSME4-induced changes in proteasome function restrict cleavage activities and antigenic diversity.** (A-E) Proteasome activity assays using the indicated fluorogenic substrate. Relative fluorescence (RFU) of the substrate is shown across the 3.5 hours of the experiment (top) or at the endpoint (bottom). A549 lysates were treated with TNF $\alpha$  and IFN $\gamma$  (T+I; red) or untreated (blue) and recombinant PSME4 was added to the lysate where indicated (paired T-test; \*\*P < 0.01, \*\*\*\* P < 0.0001). (F) Proteasome complexes were immunoprecipitated (IP) with the indicated antibody from A549 cells that were either treated with TNF $\alpha$  and IFN $\gamma$  or left untreated and blotted for the indicated proteasome subunits. (G) MAPP identified peptides were divided based on their carboxy terminus residue. The percentage of peptides with each terminus was calculated for each sample and normalized across patients. Amino acids are annotated with their GRAVY (grand average of hydropathy) score, biochemical properties and matching cleavage activity; rows are clustered using Pearson distances. (H – J) The c terminal residue of the peptides was used to classify them based on the proteasome activity attributed to their cleavage. The abundance of PSME4 in the samples based on WC proteomics correlated with the caspase-like signature (H; spearman rho = 0.69) and the chymotryptic-like signature (I; spearman rho = 0.33) and was anti-correlated with the tryptic-like signature (J; spearman rho = -0.46). (K) The percentage of each amino acid in the carboxy terminus of the differential peptides presented in the A549 cells overexpressing PSME4 (PSME4 OE; y-axis) is plotted against empty vector control (PSME4 WT; x-axis). Residues are colored based on the associated cleavage activity and a dotted line is shown for X=Y. (L-M) The percentage of each amino acid at each



peptide residue is shown. The first through seventh position (pos1 – pos7) as well as the carboxy terminus of each peptide (end) is shown for both the peptides more abundant in the PSME4 WT (L) or PSME4 OE (M) immunopeptidome. (N) The cumulative percentage of peptides explained by each additional amino acid type (from one amino acid to all twenty) is shown for the second peptide position (top) or carboxy terminus (end position, bottom). Each graph compares between peptides more abundant in the PSME4 WT (WT, red) or PSME4 OE (OE, grey) immunopeptidome.

---

well as the 19S and PSME1 regulatory caps (Fig. 2F and S6). We further confirmed the presence of hybrid PSME4-20S-PSME1 proteasomes by reciprocal immunoprecipitation with a PSME1-specific antibody (Fig. 2F and S6). Notably, when both recombinant PSME1 and PSME4 were added to cellular lysates, we observed inhibition of all measured proteasome activities (Fig. S7). Taken together, our results indicate that PSME4 attenuates immunoproteasome-associated cleavage under inflammatory conditions, thereby restricting proteasome function.

We next sought to examine whether the observed biochemical effect of PSME4 can be detected in the NSCLC clinical cohort. To that end, we analyzed the proteasome cleavage sites in the degradome. We found that the amino acid composition of the carboxy terminal residue of the degraded peptides differed between the tumor and adjacent samples (Fig. 2G). Notably, caspase- and chymotryptic-like cleavage positively correlated with the abundance of PSME4, while tryptic-like cleavage negatively correlated with it (Fig. 2H to J). As proteasome-cleaved peptides serve as the major source of class I MHC antigens and changes in cleavage can affect presentation (16, 17, 55, 56), we hypothesized that PSME4 may alter antigen presentation. Next, we performed HLA immunopeptidomics of A549 cells with PSME4 overexpression (OE) compared to control. We identified 463 peptides that were significantly changed upon PSME4 OE (Fig. S8A and B, Table S5). As caspase-cleaved peptides do not bind well to the MHC haplotypes in A549, they are not highly presented in either condition. However, the percentage of peptides with tryptic termini were decreased (Fig. 2K), corresponding with the PSME4-induced changes to the cellular degradome. (Fig. 2H to J). When examining the distribution of amino acids across the differentially presented peptides we found that the peptides presented in the PSME4 OE are less diverse than those in the A549 control cells (Fig. 2L and M). Specifically, while only 4 residues make up 80% of the peptide carboxy termini in the PSME4 OE, 9 residues describe the same percentage of peptides in the control A549 immunopeptidome, restricting the observed diversity of presented antigens (Fig. 2N and S8C). Examining the protein source of the presented peptides, we observed an enrichment of nuclear proteins in the immunopeptidome following PSME4 overexpression (Fig S8D). This is consistent with increased degradation of nuclear proteins in the cancer degradome. Thus, our results suggest that PSME4 modulates proteasome activity and thereby decreases the diversity of the cellular immunopeptidome.

To gain insight into the functional consequences of PSME4 upregulation in NSCLC, we stratified patient tumors based on their PSME4 expression levels and associated it with cellular functions. We found that PSME4-high tumors were enriched with pathways related to cell cycle and DNA replication (Fig S9), whereas PSME4-low



tumors were associated with many immune-related pathways (Fig. 3A). Proteomic analysis of PSME4-deficient A549 cells (Fig. 3B and C and S10A to B, Table S6) revealed that IFN signaling pathways were enriched following stimulation (Fig. 3D and S10C to E). By contrast, KRAS signaling and epithelial to mesenchymal transition (EMT) pathways were enriched in control conditions (Fig. S10F). Validation by qPCR showed significant increase in the expression of genes downstream to these signaling pathways, such as IFN inducible genes IFIT1 and ISG15 in PSME4-deficient cells (Fig. 3E). Interestingly, while STAT1 and STAT2 were more abundant than in the PSME4-depleted cells, STAT3 and STAT5 were reduced (Fig. 3F and S10G). STAT1 and STAT3 have previously been shown to play opposing roles in cancer-related inflammation with STAT3 serving a pro-oncogenic role (57). Consistent with this, we also observed a decrease in IL-6 expression upon PSME4 depletion, a hallmark of STAT3 signaling (Fig. 3G).

As immunoproteasome expression was previously shown to be induced by IFN (24–26) we speculated that PSME4 may impact the transcriptional regulation of the immunoproteasome. Consistent with this, by comparing the expression pattern of proteasome subunits across 1129 patients in the NSCLC TCGA cohort (TCGA-LUAD), we found that PSME4 was anti-correlated with both the core and regulatory particles of the immunoproteasome with PSMB10 being the most anti-correlated immunoproteasome subunit (Fig. 3H). To further substantiate this and examine whether there might be a causal relationship between PSME4 and immunoproteasome expression, we examined the response to TNF $\alpha$  and IFN $\gamma$  induction in PSME4-deficient cells. We found that both the catalytic and regulatory subunits of the immunoproteasomes were increased upon loss of PSME4 (Fig. 3I-J and S11A to B). Indeed, PSME4-depleted cells exhibited reduced caspase-like activity, which is associated with PSME4 (Fig S11C). The marked change in cleavage specificities together with the inflammatory signature associated with PSME4 depletion suggested it may have a direct effect MHC levels on the cell surface (16, 56, 58, 59). Indeed, we could show by FACS analysis that PSME4-depleted cells exhibited a significant increase of 30% in surface MHC I expression (Fig 3K to L and S12). Collectively, our findings highlight a role for PSME4 in regulating immunoproteasome expression and modulating downstream activation of IFN signaling, suggesting that PSME4-capped proteasomes may play an anti-inflammatory role in NSCLC.

Our findings raise the intriguing possibility that, similar to the association of high expression of immunoproteasome with an inflamed ‘hot’ tumor state (Fig. S13 and S14), a ‘cold’ tumor state may be defined in correlation to increased PSME4 expression in NSCLC. In support of this hypothesis, we found that tumors with high expression of PSME4 exhibited significantly lower T cell inflammation signature (Fig. S13 and S14) in NSCLC, suggesting PSME4 may modulate anti-tumor immunity and the response to immunotherapy. Furthermore, in melanoma, immunoproteasomes were positively associated with response to ICI (15, 60) and indeed, we could not detect any change in PSME4 abundance (Fig. S15). However, since PSME4 anti-correlates with the immunoproteasome in NSCLC, we hypothesized that the balance between PSME4 and immunoproteasome may affect the response to ICI.

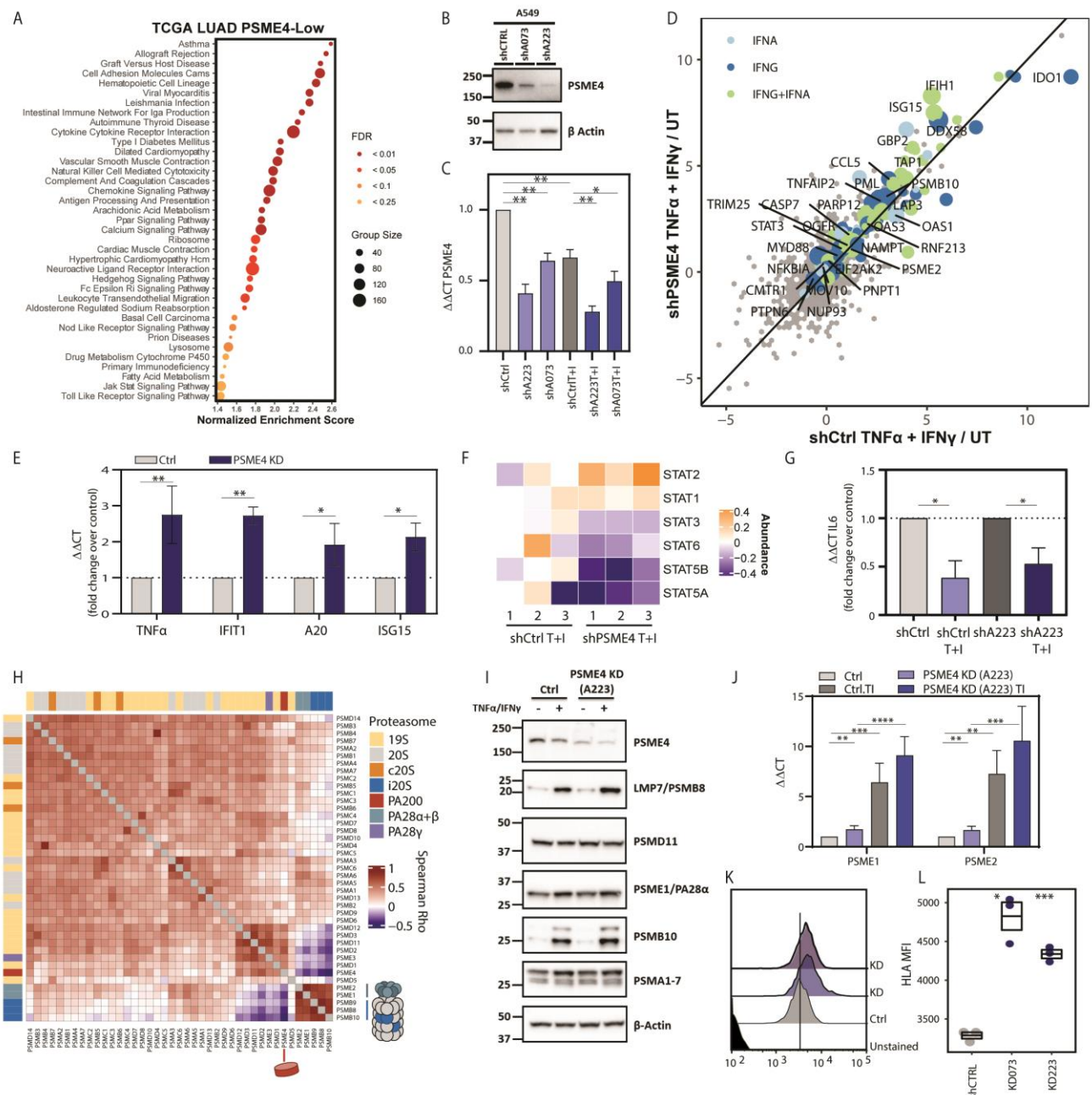


**Fig. 3 PSME4 attenuates cellular inflammation and antigenicity.** (A) The TCGA LUAD samples were stratified by PSME4 expression and PSME4- high samples were compared to PSME4- low (n = 230 samples). The normalized enrichment score for KEGG pathways significantly overrepresented in PSME4-low samples are shown. Dot color indicates FDR threshold and size indicates number of genes in the pathway (Group Size). (B) Lysates of A549 cells with PSME4 knockdown (shA223 and shA073) or control (shCtrl) were blotted for PSME4 and  $\beta$ -Actin as a loading control. (C) qPCR of PSME4 in A549 cell line following depletion of PSME4 with shA223 or shA073 compared to shCtrl with and without stimulation with TNF $\alpha$  and IFN $\gamma$  (paired T test  $^{**}P < 0.01$  and  $^{*}P \leq 0.05$ ). (D) The log<sub>2</sub> transformed ratio of protein abundances following stimulation with TNF $\alpha$  and IFN $\gamma$  compared to unstimulated (UT) is shown for PSME4 depleted A549 cells (shPSME4, y-axis) and control (shCtrl, x-axis). Proteins involved in IFN signaling are marked. Point size indicated significance of the difference between shCtrl+TI and shPSME4+TI. Points which significantly differed in the two conditions (student's t test  $P \leq 0.05$ ) are labeled with the gene name. (E) qPCR of genes downstream IFN $\gamma$  activation (TNF $\alpha$ , IFIT1, A20 and ISG15) following stimulation with TNF $\alpha$  and IFN $\gamma$ . Cells infected with shPSME4 are compared to shCtrl in A549 cell line (paired T test  $^{**}P < 0.01$  and  $^{*}P \leq 0.05$ ). (F) Abundance of STAT proteins from shPSME4 or shCtrl infected cells stimulated with TNF $\alpha$  and IFN $\gamma$ . (G) qPCR of IL6 following stimulation with TNF $\alpha$  and IFN $\gamma$  or unstimulated. Cells infected with shPSME4 are compared to shCtrl in A549 cell line

(students' T test  $*P \leq 0.05$ ). **(H)** The pairwise spearman correlation of the proteasome subunits across the TCGA LUNG cohorts ( $n = 1027$ ). Color annotations indicate subunit identity. **(I)** A549 lysates from shPSME4 or shCtrl infected cells stimulated with  $TNF\alpha$  and  $IFN\gamma$  or untreated were blotted for the indicated proteasome subunits and  $\beta$ -Actin as a loading control. **(J)** qPCR of proteasome regulators PSME1/2 in A549 cell line with PSME4 KD or shCtrl (Ctrl) following stimulation with  $TNF\alpha$  and  $IFN\gamma$  (TI) or untreated. The treatments are normalized to the untreated shCtrl in A549 cell line (Welch's corrected T test  $**P < 0.01$  and  $***P < 0.001$ ,  $****P < 0.0001$ ). **(K-L)** Histogram (L) and median fluorescence intensity (M) from fluorescence-activated cell sorting (FACS) analysis of MHC-I expression using a pan HLA-A/B/C antibody (W6/32) for A549 cells with PSME4 knockdown (shA223 and shA073) or control (shCtrl). The HLA mean fluorescent intensity (MFI) is significantly higher in the PSME4 knockdown compared to the control ( $*P = 0.01$ ,  $***P = 0.0001$ ).

---

To that end, we utilized Ex-Vivo Organoid Culture (EVOC; see materials and methods) which contains both tumor tissue and infiltrating lymphocytes (Fig 4A). We assessed the expression of PSME4 and PSMB10 from the frozen tissues prior to ICI treatment of lung tumor organoids. Following this, the same samples were treated with either Durvalumab alone ( $\alpha PD-L1$ ), or combined with Ipilimumab ( $\alpha CTLA-4$ ) and  $CD8^+$  T cell infiltrates and PDL1 levels were assessed (Fig. S16A to B). In cases where  $IFN\gamma$  was significantly enriched by at least 1.9-fold induction the EVOCs were designated as “responders” to ICI while the rest were termed “non-responders”. We found that the EVOCs that responded to the therapy had significantly lower PSME4/PSMB10 expression ratios (Fig. 4B), while neither PSME4 nor PSMB10 alone were sufficient to predict responsiveness (Fig. S16C to D). When examining the tissue-specific expression of PSME4 and PSMB10 we observe that both are expressed in the epithelial tissue, while PSMB10 was more highly expressed in the lymphocyte infiltrates consistent with the tissue expression patterns of the immunoproteasome (Fig. 4C and S17). Importantly, this relationship between expression of PSME4 and the immunoproteasome, varies greatly in different cancer types (Fig. 4D), suggesting that PSME4 expression may be an important factor in ICI therapy, beyond NSCLC.

Finally, to determine the effect of PSME4 on tumor infiltration *in vivo*, we utilized the KP1.9 cells (KrasG12D; P53<sup>-/-</sup> murine lung adenocarcinoma cells) in an orthotopic mouse model. We established isogenic cell lines of the KP1.9 either with ectopic expression or virally-induced knockdown of PSME4 (KP1.9<sup>PSME4 KD</sup>) to examine PSME4-dependent effects on tumor growth. Mice bearing KP1.9 tumors overexpressing PSME4 (KP1.9<sup>PSME4 OE</sup>) showed marked reduction in weight within 33 days from tumor cell injection, as compared to the KP1.9 tumors (Fig. 4E and S18). Further, lungs of KP1.9<sup>PSME4 OE</sup> mice were significantly larger, containing numerous lesions and metastases (Fig. 4F to H) whereas the KP1.9<sup>PSME4 KD</sup> lungs did not show any detected lesions (Fig. 4I and S19). As these effects were not driven by a change in proliferation rate (Fig. S20A), we sought to examine whether they may be mediated by anti-tumor immunity. We analyzed tumor infiltration in the KP1.9<sup>PSME4 OE</sup> tumor versus the KP1.9 counterparts as there were no tumors in the KP1.9<sup>PSME4 KD</sup>. Our analysis revealed an increase in  $PD1^+ CD8^+$  T cells (Fig. 4J and S20B) and a decrease in  $IFN\gamma$  in the tumor infiltrating lymphocytes (TILs) in KP1.9<sup>PSME4 OE</sup> tumor-bearing mice (Fig. 4K to L), suggesting decreased tumor inflammation. Furthermore, we observed a decrease in naïve  $CD8^+$  T cells ( $CD62L^+$ ,  $CD44^-$ ) and an increase in  $CD62L^-$ ,  $CD44^+$  cells, which reflect an early activator

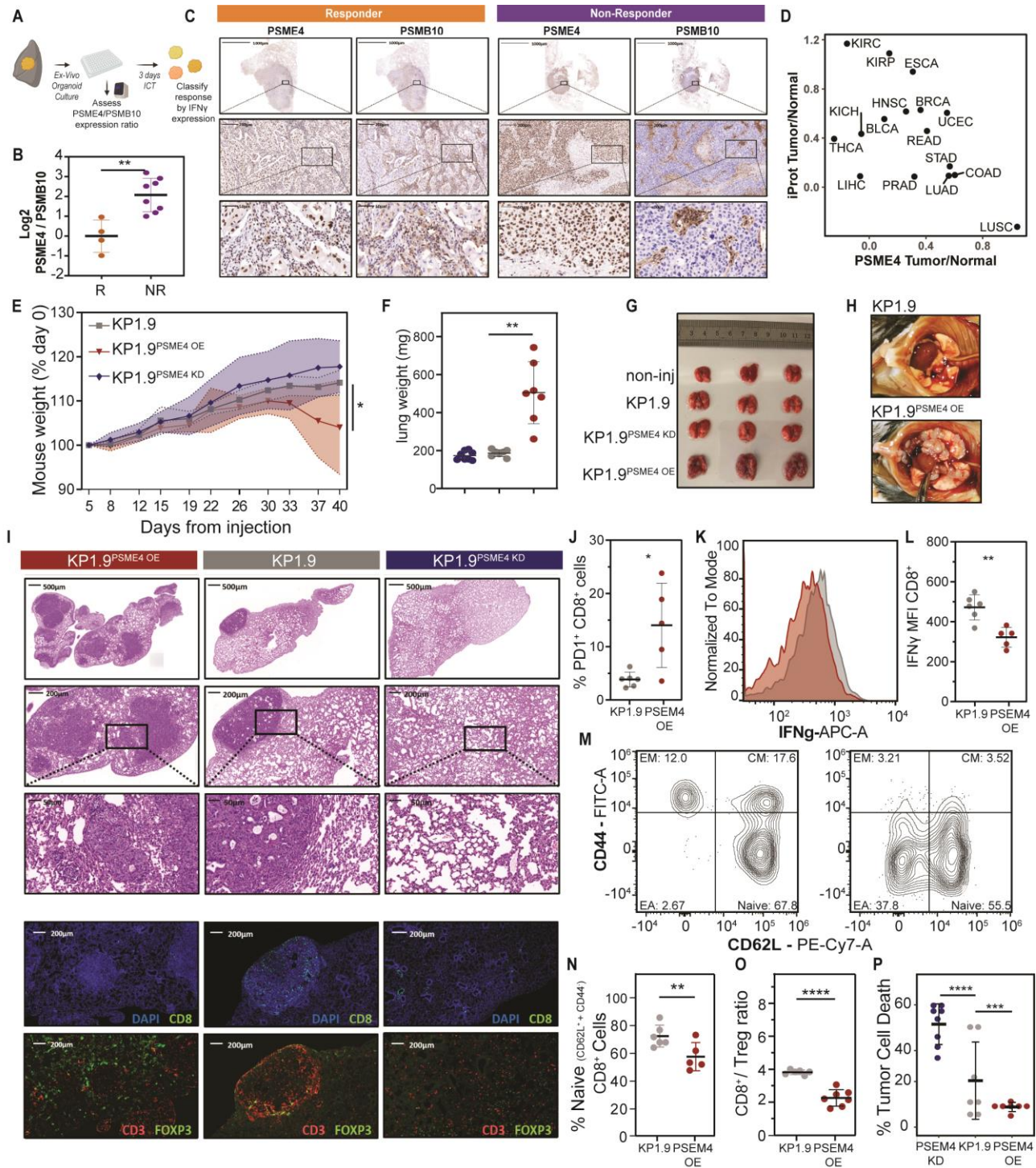


**Fig 4. PSME4 abrogates anti-tumor immunity reflecting immunotherapy efficacy.** (A) Workflow of the Ex-Vivo Organoid Culture System (EVOC). Resected tumors were assessed for PSME4 and PSMB10 expression using quantitative PCR. Then were treated for 3 days with immune checkpoint inhibitors (ICI) and responders were classified by high IFN $\gamma$  expression. (B) qPCR shows the ratio of PSME4 to PSMB10 expression in patients responding to ICI is significantly lower than non-responders (\*\* P = 0.0056). (C) Immunohistochemistry of resected tumors from an ICI responder and non-responder EVOC samples. Staining for PSME4 and PSMB10 is shown. (D) The ratio of PSME4 expression in the tumor versus normal tissue from the indicated TCGA cohort is plotted against the



ratio of the mean of the immunoproteasome (iProt) subunits PSMB8-10 and PSME1-2. **(E)** Weights of mice bearing KP1.9 wild type (KP1.9), PSME4 overexpressing (KP1.9<sup>PSME4 OE</sup>) or PSME4 KD (KP1.9<sup>PSME4 KD</sup>) orthotopic tumors injected to C57/B6 mice (n = 7-8 per group). Weights are normalized to the starting weight of each mouse. Overexpression shows significantly decreased weight as a proxy for increased disease severity (matched 2-way ANOVA \*p = 0.0322). **(F - H)** Mice bearing PSME4 overexpressing (OE) tumors showed significantly increased lung weight (\*\*P = 0.0020) and larger tumors (F) with visibly increased growth and tumor burden (G-H) compared to the control KP1.9 tumors. **(I)** H&E and immunofluorescence staining of lungs from mice bearing KP1.9, KP1.9<sup>PSME4 OE</sup>, or KP1.9<sup>PSME4 KD</sup> tumors. Tumors are stained with the antibodies indicated. **(J)** The percent of PD1 positive CD8 T cells in the lungs of the mice bearing KP1.9<sup>PSME4 OE</sup> tumors was significantly increased compared to KP1.9 tumors (\*P = 0.0440). **(K-L)** A histogram of IFN $\gamma$  stained CD8 T cells (K) shows the median fluorescent intensity (MFI) of in the lungs of the mice bearing KP1.9<sup>PSME4 OE</sup> tumors was significantly decreased compared to KP1.9 (L; \*P = 0.0017). **(M-N)** The percent of CD8 Tumor infiltrating lymphocytes (TILs) which are CD62L and/or CD44 positive in the lungs of mice bearing KP1.9<sup>PSME4 OE</sup>, KP1.9<sup>PSME4 KD</sup> or KP1.9 tumors compared to mice not bearing tumors (non-inj; M). Significant decreases in the naïve T cell population was observed in the TILs from the KP1.9<sup>PSME4 OE</sup> tumors (\*\*P<0.01, \*\*\*\*P<0.0001; N). **(O)** The ratio of CD8 T cells to Tregs was significantly decreased in the spleens of mice bearing KP1.9<sup>PSME4 OE</sup> tumors compared to KP1.9 (\*\*\*\*P <0.0001). **(P)** Splenic lymphocytes from mice bearing KP1.9, KP1.9<sup>PSME4 OE</sup> or KP1.9<sup>PSME4 KD</sup> tumors were co-cultured with KP1.9 cells. There was a significant increase in killing of KP1.9 cells co-cultured with splenic lymphocytes from KP1.9<sup>PSME4 OE</sup> bearing mice compared to KP1.9 (\*\*\*\*P <0.0001). Further, killing was reduced in the mice bearing KP1.9<sup>PSME4 OE</sup> (\*\*P = 0.002063)

---

phenotype (Fig. 4M to N and S21). Coupled with a decrease in CD8<sup>+</sup> T cell/Treg ratio in the KP1.9<sup>PSME4 OE</sup> tumors (Fig 4O), our results suggest that elevated levels of PSME in the tumor cells induce immune suppression and reduced cytotoxicity. Furthermore, in immunofluorescence staining of the lungs we could see that CD8<sup>+</sup> T cells were excluded from the KP1.9<sup>PSME4 OE</sup> tumors compared to the level of infiltration in KP1.9 tumors (Fig 4I bottom panels). Finally, we found that primed splenic lymphocytes exposed to the KP1.9<sup>PSME4 OE</sup> tumors exhibited reduced tumor killing propensity (Fig. 4P and S22) as observed by reduced cell number. By contrast, we could show that priming of splenic lymphocytes with KP1.9<sup>PSME4 KD</sup> tumors improved T-cell mediated cytotoxicity. In fact, KP1.9<sup>PSME4 KD</sup>-derived splenic lymphocytes exhibited better killing than their KP1.9 control lymphocytes, indicating that the anti-tumor activity we observed was indeed dependent on loss of PSME4.

## Discussion

In the present study, we characterized the degradation landscape in NSCLC. We utilized proteasome footprinting (46, 47) to reveal distinct degradation signatures that were shared among patients and were associated with the cancerous tissue. Notably, 10% of our degradation targets were not detected by whole cell proteomics of the same samples, suggesting that these targets may be synthesized and then rapidly degraded by proteasomes. Such ‘shared targets’ may serve as putative antigens, which may be further examined for their potential in anti-cancer vaccines (61–64). Beyond specific degradation targets, our analysis revealed that the cancerous lung tissue had increased proteasomal activity as well as altered proteasome composition, when compared to adjacent controls. We found PSME4, a proteasome subunit that was previously shown to play a role in targeting acetylated histones to degradation in the context of spermatogenesis and DNA damage response (33, 34, 36, 38, 39), to be significantly upregulated in NSCLC and to be associated with poor survival. As PSME4 expression is correlated with smoking,

we speculate that it may be upregulated to offer a protective mechanism to cope with the associated proteotoxic stress and DNA damage (51, 65–67). While label-free quantitative MS analysis of cell lines suggested that <5% of 20S proteasomes bear PSME4 regulators (41, 43), our results suggest that in NSCLC this frequency is increased to have a dominant effect on the degradation landscape. Nevertheless, this effect may be tumor-type specific as certain types of cancer such as LUAD, SCAD, and COAD are associated with increased levels of PSME4, while others like GBM and melanoma, were not.

Extending our analysis to determine the functional consequences of PSME4 upregulation we could show, for the first time, that it binds the immunoproteasome to generate a PA28-20S-PSME4 hybrids, which may serve an anti-inflammatory role. While PSME4 alters the conformation of constitutive 20S proteasomes (45), which we and others have found to amplify the  $\beta$ 1 caspase-like activity (36), we see that the counterpart  $\beta$ 1i activity is decreased upon PSME4 binding. This, in turn, attenuates immunoproteasome-associated activity. Notably, our data also suggest that PSME4 restricts proteasome activity, thereby altering the HLA landscape. It will be interesting to examine how these alterations in the presented repertoire of MHC I antigens relate to the immune suppression observed in PSME4-high tumors. As increased presentation of nuclear antigens was shown to reduce tumor immunogenicity (49), this may be another mechanism by which PSME4 modulates tumor-immune interactions. Notwithstanding the importance of antigenic peptides, we show that the altered proteasome composition in NSCLC plays detrimental role in reshaping the tumor environment by restricting immunoproteasome activity and attenuating IFN signaling. Interestingly, as PSME4 does not have a known ubiquitin recognition domain like the 19S regulatory complex, it remains to be studied if the effect we see is ubiquitin-dependent.

As immunoproteasome deficiency has been reported in NSCLC (13, 14), it will be intriguing to determine whether PSME4 may be a contributing factor. Notably, immunoproteasome deficiency was reported to be involved in EMT in lung cancer (13). Our study further suggests that the antagonistic interaction of PSME4 and the immunoproteasome is associated with pro-oncogenic and EMT pathways. Just like immunoproteasome expression has been recently shown to correlate with tumor infiltration and with the response to immune-checkpoint blockade therapy (10, 13, 15), our data suggest that the expression of PSME4 may designate ‘cold tumors’, driving tumor progression and limiting the response to immune therapy. It will be important to examine the effect PSME4 may have on different phenotypes of cancer cells and on the immune system and its interactions with tumor cells, in different cancer types. Finally, our findings highlight the degradation landscape and the interplay between different regulatory and catalytic subunits as an understudied factor in cancer proteostasis (8, 10, 13–16). The antagonistic interactions between PSME4 and PSME1/2 we have revealed offers novel insights into proteasomal regulation in cancer. Better understanding of how the degradation landscape may be controlled to drive response to therapy and anti-tumor immunity should pave way for novel treatment options for cancer patients.

## Materials and Methods

### **Purification of proteasome complexes.**

Tumors were mechanically disrupted and passed through a 70 µm cell strainer 93070 (SPL). Cells were lysed with 25 mM HEPES, pH 7.4, 10% glycerol, 5 mM MgCl<sub>2</sub>, 1 mM ATP, and 1:400 protease-inhibitor mixture (Calbiochem), then homogenized through freeze–thaw cycles and passed through a needle. The lysates were cleared by 30-min centrifugation at 21,130g at 4 °C. Lysates were treated with 2 mM 1,10-phenanthroline (Sigma), cross-linked with 0.5 mM DSP (Thermo Fisher Scientific) for 30 min at room temperature, and quenched in 100 mM Tris-HCl, pH 8, 5 mM L-cysteine for 10 min at room temperature. For immunoprecipitation, the lysates were then incubated with Protein G–Sepharose beads (Santa Cruz) with antibodies to PSMA1 and eluted with 100 mM Tris-HCl, pH 8, 8M urea and 50 mM DTT for 30 min at 37 °C. Subsequently, 1% trifluoroacetic acid (TFA) was added. Aliquots of each elution fraction were analyzed by SDS–PAGE to evaluate yield and purity.

### **Purification and concentration of proteasome peptides.**

A critical step in our procedure is the separation of peptides from the proteins eluted in the proteasomal pulldown. MAPP analyzes endogenously cleaved peptides, whereas the proteasome complex and associated proteins are physically excluded. Immunoprecipitated proteasomes and their encompassed peptides were loaded on tC18 cartridges (Waters) that were prewashed with 80% acetonitrile (ACN) in 0.1% TFA, then washed with 0.1% TFA only. After loading, the cartridges were washed with 0.1% TFA. Peptides were eluted with 30% ACN in 0.1% TFA. Protein fractions were eluted with 80% ACN in 0.1% TFA. Mass Spectrometry

### **Mass spectrometry sample processing and analysis**

Protein fraction after proteasome purification; Samples were loaded onto 3 kDa molecular weight cut-off spin columns. Volume was reduced to 25µL by centrifugation at 14,000g for 10min. 175µL 8M urea was added and centrifuged at 14,000g for 10min. Filters were reversed and centrifuged to extract the proteins. Proteins were reduced with 5 mM dithiothreitol (Sigma) for 1hr at room temperature, and alkylated with 10 mM iodoacetamide (Sigma) in the dark for 45 min at room temperature. Samples were diluted to 2M urea with 50mM ammonium bicarbonate. Proteins were then subjected to digestion with trypsin (Promega; Madison, WI, USA) overnight at 37°C at 50:1 protein:trypsin ratio, followed by a second trypsin digestion for 4 hr. The digestions were stopped by addition of trifluoroacetic acid (1% final concentration). Following digestion, peptides were desalted using Oasis HLB, µElution format (Waters, Milford, MA, USA). The samples were vacuum dried and stored in -80°C until further analysis.

Total proteomics; Lysates in 5% SDS in 50 mM Tris-HCl were incubated at 96 °C for 5 min, followed by six cycles of 30 s of sonication (Bioruptor Pico, Diagenode, USA). Proteins were reduced with 5 mM dithiothreitol



and alkylated with 10 mM iodoacetamide in the dark. Each sample was loaded onto S-Trap microcolumns (Protifi, USA) according to the manufacturer's instructions. In brief, after loading, samples were washed with 90:10% methanol/50 mM ammonium bicarbonate. Samples were then digested with trypsin for 1.5 h at 47 °C. The digested peptides were eluted using 50 mM ammonium bicarbonate; trypsin was added to this fraction and incubated overnight at 37 °C. Two more elutions were made using 0.2% formic acid and 0.2% formic acid in 50% acetonitrile. The three elutions were pooled together and vacuum-centrifuged to dry. Samples were kept at -80 °C until analysis.

HLA immunopeptidomics was performed as described previously (16, 68).

### **Liquid chromatography mass spectrometry**

Peptide fraction; ULC/MS grade solvents were used for all chromatographic steps. Each sample was loaded using split-less nano-Ultra Performance Liquid Chromatography (10 kpsi nanoAcquity; Waters, Milford, MA, USA). The mobile phase was: A) H<sub>2</sub>O + 0.1% formic acid and B) acetonitrile + 0.1% formic acid. Desalting of the samples was performed online using a reversed-phase Symmetry C18 trapping column (180 µm internal diameter, 20 mm length, 5 µm particle size; Waters). The peptides were then separated using a T3 HSS nano-column (75 µm internal diameter, 250 mm length, 1.8 µm particle size; Waters) at 0.35 µL/min. Peptides were eluted from the column into the mass spectrometer using the following gradient: 4% to 35%B in 120 min, 35% to 90%B in 5 min, maintained at 90% for 5 min and then back to initial conditions.

The nanoUPLC was coupled online through a nanoESI emitter (10 µm tip; New Objective; Woburn, MA, USA) to a quadrupole orbitrap mass spectrometer (Q Exactive Plus, Thermo Scientific) using a FlexIon nanospray apparatus (Proxeon).

Data was acquired in data dependent acquisition (DDA) mode, using a Top10 method. MS1 resolution was set to 70,000 (at 400m/z), mass range of 375-1650m/z, AGC of 3e6 and maximum injection time was set to 100msec. MS2 resolution was set to 17,500, quadrupole isolation 1.7m/z, AGC of 1e5, dynamic exclusion of 40sec and maximum injection time of 150msec.

### **Mass spectrometry data analysis.**

Raw data were analyzed in MaxQuant software (version 1.6.0.16) with the default parameters for the analysis of the proteasomal peptides, except for the following: unspecific enzyme, LFQ minimum ratio count of 1, minimum peptide length for unspecific search of 6, maximum peptide length for unspecific search of 40, and match between runs enabled. A stringent false discovery rate (FDR) of 1% was applied for peptide identification (in accordance with the FDR reported in a previous peptidomics study). For the analysis of tryptic digests, the default parameters

were set, apart from a minimum peptide length of 6. Masses were searched against the human proteome database from UniprotKB (last update September 2018).

### **Proteomics processing and label-free quantification.**

Peptides resulting from MaxQuant were initially filtered to remove reverse sequences and known MS contaminants. For MAPP peptide fraction we removed antibody and proteasome peptides as contaminants. To decrease ambiguity, we allowed peptides that had at least two valid LFQ intensities out of sample replicates, and we included razor peptides, which belong to a unique MaxQuant 'protein group'. MAPP protein intensities were inferred with MaxQuant. For graphical representation, intensities were log transformed, and in Python v3.6, zero intensity was imputed to a random value chosen from a normal distribution of 0.3 s.d. and downshifted 1.8 s.d. For clinical cohorts, zero intensity was imputed to half the minimum. In cases of matched samples ratios were calculated per pair and paired t tests were used. Otherwise, ratios were calculated based on the median of each group and a non-paired student t test was used. The protein fraction of the MAPP analysis was normalized to the mean of the core proteasome subunits (PSMA1-7 and PSMB1-4) to control for efficiency. For the immunopeptidomics, values from a peptide that was not detected in a treatment pair were not included in the analysis. The binding of peptides was predicted by netMHC based on A549 haplotypes as described previously(56). Any peptide with a binding rank greater than 5 was considered as a contaminant for analysis of the differentially presented peptides.

### **TCGA and CPTAC analysis.**

The cancer genome atlas (TCGA) data was mined using the xenaPython package in Python 3.6. The results shown in this analysis are in whole or part based upon data generated by the TCGA Research Network: <http://cancergenome.nih.gov/>. The full lung carcinoma cohort (both lung adenocarcinoma [LUAD] and lung squamous cell carcinoma [LUSC] designations, n = 1129) or the LUAD cohort alone (n = 576) as indicated. For the cross-cancer proteasome ratio the GDC pan cancer dataset was used. Only types with 10 or more normal controls were used. Ratios presented are the difference between the means of the normal and tumor groups. Data used in this publication were generated by the Clinical Proteomic Tumor Analysis Consortium (NCI/NIH). The CPTAC LUAD cohort (n = 213) was used. In cases where ratios between the adjacent and tumor samples are presented only those samples with matching controls are used. Otherwise all the tumor and normal (adjacent control) samples were utilized. The DNA repair signature was taken from CancerSEA and the T cell inflammation signature was based on Spranger et al. (69, 70).

### **Statistical analysis and data visualization.**

Statistical analyses were performed in R v 3.6.2 and GraphPad Prism v 7.04. In R data was visualized using the complexheatmap (71) and ggplot (72) packages. Defaults were used unless otherwise noted. Protein annotation and gene ontology analysis were performed with the gene-set enrichment analysis and protein subcellular localization was extracted from the Human protein atlas (73–75) with “uncertain” or “approved” localization reliabilities excluded.

### **Antibodies and plasmids**

Rabbit anti PSME4 HPA060922 1:1000 WB, 1:300 IF (Sigma)

Rabbit anti PSMD11 ab99414 1:1000 WB, Mouse anti proteasome 20s PSMA1-7 subunits ab22674 1:1000 WB, Rabbit anti PSMB10/MECL1 ab183506 1:1000 WB, Mouse anti  $\beta$  Actin ab170325 1:5000 WB (Abcam), Rabbit anti PA28alpha/PSME1 9643 1:1000wb, Rabbit anti PSMB8/LMP7 13635 1:1000 WB (Cell Signaling)

Mouse anti alpha-6, produced from hybridoma was a kind gift from Keiji Tanaka. IgG1k isotype antibody (BioLegend, BLG-400139) was used as a control of MAPP method.

Goat anti Mouse 488 A11029 1:400, Goat anti mouse 647 A31571 1:400 (Invitrogen), Goat anti Rabbit 647 AB150075 1:400 (Abcam), Goat anti mouse HRP 115-035-205 1:5000, Goat anti Rabbit HRP 111-035-003 1:5000 (Jackson labs).

MISSION shRNA targeting mouse or human PSME4 or RFP were obtained from Sigma (TRCN0000176569, TRCN0000178428, TRCN0000158223, TRCN0000157072)

pcDNA3.1\_PSME4(68) was transfected into A549/KP1.9 cells with Lipofectamine 2000 (Thermo Fisher).

### **Cell culture and drug treatments**

A549 were originally obtained from ATCC grown in DMEM and used as model systems for cell biology studies including western blot, biochemistry, and imaging. KP1.9, kindly provided by Alfred Zippelius, were grown in Iscove's MDM. Cells were routinely tested for mycoplasma contamination. Media were supplemented with 10% fetal bovine serum, 1% Penicillin/streptomycin and L-glutamine (2mmol/l) (Biological industries), unless otherwise indicated, at 37 °C with 5% CO<sub>2</sub>.

For TNF- $\alpha$ /IFN- $\gamma$  activation cells were allowed to seed overnight, and subsequently treated with TNF- $\alpha$  (PeproTech, 300-01A) and IFN- $\gamma$  (PeproTech, 300-02) at 20 ng/ml and 10 ng/ml, respectively, for 24h.

Cell death assessment was done by trypan blue staining and counted with Countess II™ automated cell counter (Thermo Fisher) and by Cell titerGlo assay (Promega). Proliferation of mammalian cells was measured by KIT8 assay (Sigma).

Concentrations of cell treatments: 100 µg/ml cycloheximide (CHX; Sigma) for 2 h. Epoxomicin was used at a concentration of 1 µM for 4 h

### **Proteasome cleavage reporter assay**

Cells were lysed with 25 mM HEPES, pH 7.4, 10% glycerol, 5 mM MgCl<sub>2</sub>, 1 mM ATP, and 1:400 protease-inhibitor mixture (Calbiochem), then homogenized through freeze–thaw cycles and passed through a needle. The lysates were cleared by 30-min centrifugation at 21,130g at 4 °C to remove cell debris. Protein concentration of the supernatant was determined by a NanoDrop spectrophotometer (Thermo Fisher Scientific) by measuring the absorbance at 280 nm.

Proteasomal activity in cell fractions was determined by cleavage of the fluorogenic precursor substrate Suc-Leu-Leu-Val-Tyr-AMC (Suc-LLVY-AMC), Ac-Pro-Ala-Leu-AMC (Ac-PAL-AMC), Z-Leu-Leu-Glu-AMC (Z-LLE-AMC), Ac-Arg-Leu-Arg-AMC (Ac-RLR-AMC), Ac-Ala-Asn-Trp-AMC (Ac-ANW-AMC) (Boston Biochem), Z-Leu-Leu-Glu-βNA (Z-LLE-βNA), Ac-Nle-Pro-Nle-Asp-AMC (Ac-nLPnLD-AMC) (Bachem). 10 µM substrate was added to 10 µg total protein/well, and incubated in a reaction buffer (50 mM Hepes, pH 7.5, 1 mM DTT, 5 mM MgCl<sub>2</sub> and 2 mM ATP). Fluorescent increase resulting from degradation of peptide-AMC at 37°C was monitored over time by means of a fluorometer (Synergy H1 Hybrid Multi-Mode Microplate Reader, BioTek) at 340 nm excitation and at 460 nm emission, using the proteasome inhibitor, MG132 (Calbiochem) as background. Resulting product curves were followed for up to 3.5 hours. Each value of fluorescence intensity represents a mean value obtained from three independent experiments.

### **Immuno-blotting**

Cells were lysed in STET buffer (50 mM Tris-HCl, pH 8.7.5, 150 mM NaCl, 2 mM EDTA 1% Triton-X and 1:400 protease-inhibitor mixture (Calbiochem)). Protein concentration was assessed using BC Assay Protein Quantitation Kit (Interchim). 20 µg of total protein was separated by SDS–PAGE on 4-20% gradient ExpressPlus PAGE M42015 (GenScript) and transferred onto PVDF membranes using iBlot™ 2 Gel Transfer Device (Thermo Fisher Scientific). The membranes were blocked in 5% milk prepared in TBS-0.1% Tween and incubated in primary antibodies overnight at 4°C followed by washing and incubation with secondary antibody. Blots were developed using the ChemiDoc XRS+ Imaging System (Bio-Rad) and band intensities were quantified with imageJ analyzer software.

### **Immuno-precipitation**

Cells lysed in 25 mM HEPES, pH 7.4, 10% glycerol, 5 mM MgCl<sub>2</sub>, 1 mM ATP, and 1:400 protease-inhibitor mixture (Calbiochem), then homogenized through freeze–thaw cycles and passed through a needle. The lysates were cleared by 30-min centrifugation at 21,130g at 4 °C to remove cell debris. Pre-cleared cell lysates were

prepared by incubating with Protein A/G conjugated agarose beads for 30 min at 4°C with slow rotation. 1 mg Pre-cleared cell lysates were then added to 20 µL of fresh Protein A/G conjugated agarose beads along with 4 µg of antibodies (as described). The mixture was incubated over-night at 4°C with slow rotation followed by three 1 ml washes with chilled PBS buffer. The target conjugates were then eluted from beads by mixing protein loading dye (with reducing agents) and heating for 5 min at 95°C followed by denaturing Western blot.

### **Gel Filtration**

Gel filtration experiments were performed using Superose® 6 Increase 10/300 GL size exclusion column (GE Healthcare) AKTA prime automated liquid chromatography system (Amersham Biosciences). The running buffer used was 25 mM HEPES, pH 7.4, 10% glycerol, 5 mM MgCl<sub>2</sub> and 1 mM ATP. The column was calibrated using gel filtration molecular weight standard (Bio-Rad). The following standards were used for calibration:

Thyroglobulin (670 kDa,  $R_s$ =8.6 nm),  $\gamma$ -globulin (158 kDa,  $R_s$ =5.1 nm), Ovalbumin (44 kDa,  $R_s$ =2.8 nm), Myoglobin (17 kDa,  $R_s$ =1.9 nm), Vitamin B12 (1.35 kDa), and Dextran blue (2 MDa).

A 0.1 ml protein sample at a final concentration of 0.4 mg/ml was filtered and chromatographically analyzed using a flow rate of 0.5 ml/min. Absorbance was monitored at 280 nm, elution volumes were determined from UV chromatogram. The partition coefficient,  $K_{av}$ , was calculated from the elution volume of the sample,  $V_e$ , and total bed volume,  $V_t$ , using the expression:  $K_{av} = (V_e - V_0)/(V_t - V_0)$ . Calibration curves and equations were established.

### **Surface HLA staining; FACS**

A549 and KP1.9 cells were treated with hTNF $\alpha$ /hIFN $\gamma$  (as described above) or mTNF $\alpha$ /mIFN  $\gamma$ , respectively, for 24 hr. Cells were fixed and stained with Live/Dead Aqua staining kit from BioLegend as per manufacturer's protocol. Approximately  $1 \times 10^6$  cells were washed, blocked with 2% FCS for 5 min and stained with anti-HLA-A/B/C-PE (A549) or anti-MHCI-Kb-PE/MHCI-Db-FITC (KP1.9) in 100ul for 30 min. Cells were washed and acquired.

### **Tissues fixation, processing and embedding**

Tissues were fixed in 4% paraformaldehyde for one week. Dehydration of the tissue was done by serial immersion in increasing concentrations of alcohol (70 to 100%) and removal of the dehydrant with Xylene. The tissue was embedded in paraffin, sectioned at 4 µm and mounted on microscope slides. The slides were placed in an oven for one hour at 60°C or overnight at 37°C before immunohistochemically staining.

### **Immunohistochemistry (IHC) and Immunofluorescence staining**

H&E stains were performed on an automated device according to manufacturer's instructions. IHC stains were performed on a Benchmark XT staining module (Ventana Medical Systems Inc.; USA) using iVIEW DAB Detection Kit (760-091, Ventana Medical Systems Inc.) or Ultra VIEW Universal DAB Detection Kit (760-500, Ventana Medical Systems Inc.; USA). Antibody details are described above. Following immunostaining, sections were counterstained with hematoxylin (Ventana Medical Systems Inc.), rinsed in distilled water and dehydrated manually in graded ethanols. Finally the sections were cleared in xylene and mounted with Entellan (Surgipath Medical Industries Inc) on glass slides.

The immunofluorescent staining was performed at Molecular Cytology Core Facility of MSKCC using Discovery XT processor (Ventana Medical Systems). Sections were stained with antibodies for CD31 (endothelial cell marker), CD3 (T cells), CD8(T cells) and FoxP3 (Tregs).

Scanning of slides was done by PANNORAMIC SCAN II (3DHISTECH).

#### **IHC staining PA200/PSME4**

Paraffin embedded mouse and human tissues were cut in 3 µm thick sections using the Hyrax M55 microtome (Zeiss). Tissue sections were incubated for one hour at 60 °C in order to melt paraffin, deparaffinized by incubating two times in xylene for 5 min and rehydrated in a descending alcohol series (100 %, 90 %, 80 % and 70 % (v/v)) for 1 min. To block endogenous protease activity and to permeabilize sections for nuclear staining they were incubated in a methanol/hydrogen peroxide (80 %/1.8 % (v/v)) solution for 20 min. Tissue sections were rinsed in Milli-Q® water and heat-induced antigen retrieval was performed in citrate buffer pH 6 using a decloaking chamber (Biocare Medical). After washing with TBST unspecific binding sites were blocked for 30 min with Rodent Block M (Biocare Medical). The slides were washed again in TBST and incubated with anti-PSME4 antibody (sc-135512, Santa Cruz) diluted in Antibody Diluent (DAKO) for 1 h at RT. After extensive washing in TBST sections were incubated with MACH 2 Rabbit AP-Polymer (Biocare Medical) for 30 min at RT. Sections were rinsed again in TBST and incubated in Vulcan Fast Red AP substrate solution (Biocare Medical) for 10 min. Tissue sections were washed in TBST and MilliQ® water and hematoxylin counterstaining (Carl Roth) was performed to visualize nuclei. After repeated washing in TBST, sections were dehydrated in ethanol and xylene and mounted using Entellan mounting medium (Merck Millipore). Slides were imaged using the MIRAX scanning system (Zeiss).

Stainings were analyzed by an expert clinical pathologist blinded to the sample identity. Semiquantitative scores for PSME4 expression were obtained by defining the percentage of PSME4 positively stained tumor areas multiplied by the intensity of staining as graded between 1 (weak) to 3 (strong). Scores were dichotomized into high (>80) and low (<80) expressing tumors with the score 80 representing the median of all samples and PSME4 expression scores were correlated with survival of the patients for this cohort.

## q-PCR analysis

RNA was extracted using Direct-zol™ RNA MiniPrep R2051 (ZYMO research) mRNA levels were ascertained by RT using High-Capacity cDNA Reverse Transcription Kit (ThermoFisher) real time quantitative PCR using sybr-green (Kapa Biosystems) and the StepOnePlus™ Real-Time PCR Systems (Life Technologies) using the following primers:

Primers for real time PCR		
mPSME4	F	GCGTTGGCTGAACAAGTTAATG
mPSME4	R	CTCAGGTCTCATAAGTGCAAGG
hPSME4	F	ATTTGGAGTTACCCTGGAGACC
hPSME4	R	GCAGCTTTTCACGAGTGTTTTG
hPSMB10	F	TCCTTCGAGAACTGCCAAAGA
hPSMB10	R	ATCGTTAGTGGCTCGCGTATC
hPSME1	F	CCAGTGCCTGATCCAGTCAAG
hPSME1	R	ACCACGATCTTTTCATTGCAGT
hPSME2	F	GCAAGAGGACTCCCTCAATGT
hPSME2	R	CTTCTGGCTTAACCAGGGCA
hTNFa	F	CCACGTCGTAGCAAACCACC
hTNFa	R	TTGAGATCCATGCCGTTGGC
hISG15	F	GAG AGG CAG CGA ACT CAT CT
hISG15	R	CTT CAG CTC TGA CAC CGA CA
hIFIT	F	GATCAGCCATATTTTCATTTGAATC
hIFIT	R	GAAAATTCTCTTCAGCTTTTCTGTG
hIL6	F	TTCTCCACAAGCGCCTTCGGTC
hIL6	R	TCTGTGTGGGGCGGCTACATCT
hA20	F	GCGTTCAGGACACAGACTTG
hA20	R	TTCATCATTCCAGTCCGAGTATC
hRPS18	F	ATTAAGGGTGTGGGCCGAAG
hRPS18	R	TGGCTAGGACCTGGCTGTAT
hGAPDH	F	CAACGGATTGGTCGTATTG
hGAPDH	R	GATGACAAGCTTCCCCTTCT
mGAPDH	F	AAGGTCATCCCAGAGCTGAA
mGAPDH	R	CTGCTTACCACCTTCTTGA

All values were normalized to the mRNA abundance of house keeping genes (RPS18 or GAPDH in Human; GAPDH in Mouse). Each primers pair was calibrated using the Absolute Quantification program with increasing concentrations of cDNA.

## EVOC preparation

As previously described in (76)

## Orthotopic lung cancer model



Mouse experiments were conducted according to approved experimental procedures (Approval numbers 04400520-2). Male C57Bl/6 mice (Envigo, Israel) at the age of 8-10 weeks were injected i.v. with  $2 \times 10^5$  cells in 200  $\mu$ L PBS (Biological Industries, Israel). Mice were observed for adverse effects and weights noted twice a week. Peripheral blood was collected from the tail vein. At the end of experiment, mice were sacrificed by CO<sub>2</sub> asphyxiation and tissues collected to cold PBS.

### **Tissue processing and flow cytometry staining**

Peripheral blood was washed and red blood cells removed by ACK lysis buffer (150 mM NH<sub>4</sub>Cl, 10 mM KHCO<sub>3</sub>, 0.1 mM EDTA in 0.1x PBS-/-) and washed in flow cytometry buffer (PBS-/-, 0.5% BSA, 2mM EDTA).

Spleens and lungs were weighted before further processing. The left lung lobe was used for histological analysis of tumor development (hematoxylin and eosin) after fixation in 4% formaldehyde (Biolabs, Israel). Right lung lobes were minced and digested with 5 mL digestion buffer: Collagenase 4 (200U/mL, Worthington Biochemicals), DNase I (100 ug/mL, Sigma Aldrich) in PBS++ supplemented with 2 mM CaCl<sub>2</sub> for 20 minutes at 37°C under shaking. Single cell suspensions of spleen and lungs were obtained by straining cells through 100  $\mu$ m strainers and washed in cold flow cytometry buffer. Red blood cells were removed by ACK lysis buffer, washed with flow cytometry buffer and strained again.

For intracellular cytokine and transcription factor stainings, cells were incubated for 4 hours with Brefeldin A (Biolegend) and Monensin (Sigma Aldrich). First, viability staining was done with Live/Deal Aqua staining kit (Thermo Fisher Scientific) or Zombie Aqua (Biolegend) according to the protocols. Cell surface staining was performed in flow cytometry buffer in 100  $\mu$ L at appropriate dilutions (see Supp Table XXX for antibody list). When needed, cells were fixed and permeabilized with the FoxP3 transcription factor kit from eBioscience (Thermo Fisher Scientific) and stained for FoxP3 and IFN $\gamma$  according to the manufacturers protocol. Samples were acquired on an Attune Nxt with Autosampler and analyzed in FlowJo (V10.6.2, Becton, Dickinson and Company). Exemplary gating strategies are provided in Supp Fig. S21.

### **Cytotoxicity assay**

10,000 KP1.9 WT cells were stained with CFSE (5 $\mu$ M; BioLegend), at a cell concentration of  $1 \times 10^6$ /ml, plated onto a 96-well plate and allowed to attach overnight. The following day, splenocytes were isolated from naïve mice, or from mice bearing KP1.9-WT, -PSME4 KD, or -PSME4 OE tumors. Red blood cells were lysed using ACK buffer, cells were washed in PBS, and 100,000 splenocytes were plated on top of the tumor cells in RPMI medium + beta-mercaptoethanol (50 $\mu$ M). Co-culture was maintained for 7 days. On day 7, cell supernatants were collected onto a new 96-well plate, and the attached tumor cells were detached with Trypsin containing Propidium

Iodide (PI). After cell detachment, the supernatant was used to resuspend the detached cells, and the entire sample was acquired.

### **Statistics and reproducibility**

All experiments were performed in three individual replicates unless otherwise mentioned. For each experiment, all compared conditions were analyzed by MS at the same time. For the NSCLC study, eight samples from healthy individuals and eight samples from patients with SLE were analyzed. The samples were processed independently and analyzed by MS at the same time to maintain comparability across samples and decrease batch effects.

### **Ethics Statement**

Human lung tissue obtained from patients surgically treated for lung cancer was provided by the Asklepios Biobank for Lung Disease, Gauting, Germany or obtained from the Israel National Biobank for Research (MIDGAM). Samples were obtained under the approval of the Ministry of Health (MOH) IRB approval for the Israel National Biobank for Research (MIDGAM), protocol no. 118-2018 or the ethics committee of the Ludwig-Maximilians University Munich according to national and international guidelines (project number 333-10).

For the ex-vivo organoid cultures, all patients provided written informed consent for the use of blood samples and tumor specimens for research. This study was approved by the Sheba Medical Center ethics committee

### **Data availability**

The mass spectrometry proteomics data have been deposited to the ProteomeXchange Consortium via the PRIDE (77) partner repository with the dataset identifier PXD019573. (Username: [reviewer02593@ebi.ac.uk](mailto:reviewer02593@ebi.ac.uk), Password: rqPQNaZS).

### **References:**

1. P. Sharma, J. P. Allison, The future of immune checkpoint therapy. *Science* (80-. ). **348**, 56–61 (2015).
2. A. Giri, S. S. Walia, A. Gajra, Clinical Trials Investigating Immune Checkpoint Inhibitors in Non-Small-Cell Lung Cancer. *Rev. Recent Clin. Trials*. **11**, 297–305 (2016).
3. S. J. Antonia, J. F. Vansteenkiste, E. Moon, Immunotherapy: Beyond Anti-PD-1 and Anti-PD-L1 Therapies. *Am. Soc. Clin. Oncol. Educ. B*. **35**, e450–e458 (2016).
4. M. D. Wellenstein, K. E. de Visser, Cancer-Cell-Intrinsic Mechanisms Shaping the Tumor Immune

Landscape. *Immunity*. **48** (2018), pp. 399–416.

5. G. T. Gibney, L. M. Weiner, M. B. Atkins, Predictive biomarkers for checkpoint inhibitor-based immunotherapy. *Lancet Oncol.* **17** (2016), pp. e542–e551.
6. E. M. Van Allen, D. Miao, B. Schilling, S. A. Shukla, C. Blank, L. Zimmer, A. Sucker, U. Hillen, M. H. G. Foppen, S. M. Goldinger, J. Utikal, J. C. Hassel, B. Weide, K. C. Kaehler, C. Loquai, P. Mohr, R. Gutzmer, R. Dummer, S. Gabriel, C. J. Wu, D. Schadendorf, L. A. Garraway, Genomic correlates of response to CTLA-4 blockade in metastatic melanoma. *Science* (80-. ). **350**, 207–211 (2015).
7. N. Auslander, G. Zhang, J. S. Lee, D. T. Frederick, B. Miao, T. Moll, T. Tian, Z. Wei, S. Madan, R. J. Sullivan, G. Boland, K. Flaherty, M. Herlyn, E. Rupp, Robust prediction of response to immune checkpoint blockade therapy in metastatic melanoma. *Nat. Med.* **24**, 1545–1549 (2018).
8. M. Ayers, J. Lunceford, M. Nebozhyn, E. Murphy, A. Loboda, D. R. Kaufman, A. Albright, J. D. Cheng, S. P. Kang, V. Shankaran, S. A. Piha-Paul, J. Yearley, T. Y. Seiwert, A. Ribas, T. K. McClanahan, IFN- $\gamma$ -related mRNA profile predicts clinical response to PD-1 blockade. *J. Clin. Invest.* **127**, 2930–2940 (2017).
9. M. Lauss, M. Donia, K. Harbst, ... R. A.-N., U. 2017, Mutational and putative neoantigen load predict clinical benefit of adoptive T cell therapy in melanoma. *Nat. Commun.*
10. N. Riaz, J. J. Havel, V. Makarov, A. Desrichard, W. J. Urba, J. S. Sims, F. S. Hodi, S. Martín-Algarra, R. Mandal, W. H. Sharfman, S. Bhatia, W. J. Hwu, T. F. Gajewski, C. L. Slingluff, D. Chowell, S. M. Kendall, H. Chang, R. Shah, F. Kuo, L. G. T. Morris, J. W. Sidhom, J. P. Schneck, C. E. Horak, N. Weinhold, T. A. Chan, Tumor and Microenvironment Evolution during Immunotherapy with Nivolumab. *Cell*. **171**, 934-949.e15 (2017).
11. W. Hugo, J. M. Zaretsky, L. Sun, C. Song, B. H. Moreno, S. Hu-Lieskovan, B. Berent-Maoz, J. Pang, B. Chmielowski, G. Cherry, E. Seja, S. Lomeli, X. Kong, M. C. Kelley, J. A. Sosman, D. B. Johnson, A. Ribas, R. S. Lo, Genomic and Transcriptomic Features of Response to Anti-PD-1 Therapy in Metastatic Melanoma. *Cell*. **165**, 35–44 (2016).
12. R. Rosenthal, E. L. Cadieux, R. Salgado, M. Al Bakir, D. A. Moore, C. T. Hiley, T. Lund, M. Tanić, J. L. Reading, K. Joshi, J. Y. Henry, E. Ghorani, G. A. Wilson, N. J. Birkbak, M. Jamal-Hanjani, S. Veeriah, Z. Szallasi, S. Loi, M. D. Hellmann, A. Feber, B. Chain, J. Herrero, S. A. Quezada, J. Demeulemeester, P. Van Loo, S. Beck, N. McGranahan, C. Swanton, C. Swanton, M. Jamal-Hanjani, S. Veeriah, J. Czyzewska-Khan, D. Johnson, J. Laycock, R. Rosenthal, P. Gorman, R. E. Hynds, G. Wilson, N. J. Birkbak, T. B. K. Watkins, N. McGranahan, M. Escudero, A. Stewart, A. Rowan, C. Hiley, C. Abbosh, J. Goldman, R. K. Stone, T. Denner, S. Ward, E. Nye, K. Joshi, A. Ben Aissa, Y. N. S. Wong, A. Georgiou, S. Quezada, J. A. Hartley, H. L. Lowe, J. Herrero, D. Lawrence, M. Hayward, N. Panagiotopoulos, M. Falzon, E. Borg, T. Marafioti, S. M. Janes, M. Forster, T. Ahmad, S. M. Lee, D. Papadatos-Pastos, D. Carnell, R. Mendes, J. George, A. Ahmed, M. Taylor, J. Choudhary, Y. Summers, R. Califano, P. Taylor, R. Shah, P. Krysiak, K. Rammohan, E. Fontaine, R. Booton, M. Evison, P. Crosbie, S. Moss, L. Joseph, P. Bishop, A. M. Quinn, H. Doran, A. Leek, P. Harrison, K. Moore, R. Waddington, J. Novasio, F. Blackhall, J. Rogan, E. Smith, C. Dive, J. Tugwood, G. Brady, D. G. Rothwell, J. Pierce, S. Gulati, B. Naidu, G. Langman, S. Trotter, H. Bancroft, A. Kerr, S. Kadiri, G. Middleton, M. Djearaman, D. Fennell, J. A. Shaw, J. Le Quesne, D. A. Moore, A. Nakas, S. Rathinam, W. Monteiro, H. Marshall, L. Nelson, J. Riley, L. Primrose, L. Martinson, G. Anand, S. Khan, M. Nicolson, K. Kerr, S. Palmer, H. Remmen, J. Miller, K. Buchan, M. Chetty, L. Gomersall, J. Lester, F. Morgan, H. Adams, H. Davies, M. Kornaszewska, R. Attanoos, S. Lock, M. MacKenzie, M. Wilcox, H. Bell, A. Hackshaw, Y. Ngai, S. Smith, N. Gower, C. Ottensmeier, S. Chee, B. Johnson, A. Alzetani, E. Shaw, E. Lim, P. De Sousa, M. T. Barbosa, A. Bowman, S. Jordan, A. Rice, H. Raubenheimer, H. Bhayani, M. Hamilton, N. Mensah, L. Ambrose, A. Devaraj, H. Chavan, A. G. Nicholson, K. Lau, M. Sheaff, P. Schmid, J. Conibear, V. Ezhil, V. Prakash, P. Russell, T. Light, T. Horey, S. Danson, J. Bury, J. Edwards, J. Hill, S. Matthews, Y. Kitsanta, K. Suvarna, P. Fisher,

- M. Shackcloth, J. Gosney, S. Feeney, J. Asante-Siaw, K. Ryanna, A. Dawson, M. Tuffail, A. Bajaj, J. Brozik, H. Walter, N. Carey, G. Price, K. Gilbert, J. Webb, A. Patel, A. Chaturvedi, F. Granato, K. Baker, M. Carter, L. Priest, M. G. Krebs, C. Lindsay, F. Gomes, F. Chemie, R. George, D. Patrini, R. Khirya, P. Shaw, M. Skrzypski, M. W. Sunderland, J. L. L. Reading, C. Beastall, N. Mangal, K. Peggs, E. Lim, M. Al-Bakir, N. Navani, M. Scarci, L. Ensell, D. Biswas, R. Salgado, M. Razaq, J. Nicod, S. Beck, S. Lopez, A. Huebner, M. Dietzen, T. Mourikis, T. Adefila-Ideozu, S. Begum, H. Klein, A. Mani, S. Carvalho, D. Kaniu, C. Realengo, M. Malima, S. Booth, L. Lim, J. Rao, S. Tenconi, L. Socci, F. Kibutu, M. Agyemang, R. Young, K. G. Blyth, C. Dick, A. Kirk, A. Kidd, Neoantigen-directed immune escape in lung cancer evolution. *Nature*. **567**, 479–485 (2019).
13. S. C. Tripathi, H. L. Peters, A. Taguchi, H. Katayama, H. Wang, A. Momin, M. K. Jolly, M. Celiktas, J. Rodriguez-Canales, H. Liu, C. Behrens, I. I. Wistuba, E. Ben-Jacob, H. Levine, J. J. Molldrem, S. M. Hanash, E. J. Ostrin, Immunoproteasome deficiency is a feature of non-small cell lung cancer with a mesenchymal phenotype and is associated with a poor outcome. *Proc. Natl. Acad. Sci. U. S. A.* **113**, E1555-64 (2016).
  14. M. Spits, J. Neefjes, Immunoproteasomes and immunotherapy—a smoking gun for lung cancer? *J. Thorac. Dis.* **8**, E558–E563 (2016).
  15. M. Harel, R. Ortenberg, S. K. Varanasi, K. C. Mangalhara, M. Mardamshina, E. Markovits, E. N. Baruch, V. Tripple, M. Arama-Chayoth, E. Greenberg, A. Shenoy, R. Ayasun, N. Knafo, S. Xu, L. Anafi, G. Yanovich-Arad, G. D. Barnabas, S. Ashkenazi, M. J. Besser, J. Schachter, M. Bosenberg, G. S. Shadel, I. Barshack, S. M. Kaech, G. Markel, T. Geiger, Proteomics of Melanoma Response to Immunotherapy Reveals Mitochondrial Dependence. *Cell*. **179**, 236-250.e18 (2019).
  16. S. Kalaora, J. S. Lee, E. Barnea, R. Levy, P. Greenberg, M. Alon, G. Yagel, G. Bar Eli, R. Oren, A. Peri, S. Patkar, L. Bitton, S. A. Rosenberg, M. Lotem, Y. Levin, A. Admon, E. Ruppin, Y. Samuels, Immunoproteasome expression is associated with better prognosis and response to checkpoint therapies in melanoma. *Nat. Commun.* **11** (2020), doi:10.1038/s41467-020-14639-9.
  17. K. L. Rock, E. Reits, J. Neefjes, Present Yourself! By MHC Class I and MHC Class II Molecules. *Trends Immunol.* **37**, 724–737 (2016).
  18. J. Chapiro, S. Claverol, F. Piette, W. Ma, V. Stroobant, B. Guillaume, J.-E. Gairin, S. Morel, O. Burlet-Schiltz, B. Monsarrat, T. Boon, B. J. Van den Eynde, Destructive Cleavage of Antigenic Peptides Either by the Immunoproteasome or by the Standard Proteasome Results in Differential Antigen Presentation. *J. Immunol.* **176**, 1053–1061 (2006).
  19. E. S. Schultz, J. Chapiro, C. Lurquin, S. Claverol, O. Burlet-Schiltz, G. Warnier, V. Russo, S. Morel, F. Lévy, T. Boon, B. J. Van Den Eynde, P. Van Der Bruggen, The production of a new MAGE-3 peptide presented to cytolytic T lymphocytes by HLA-B40 requires the immunoproteasome. *J. Exp. Med.* **195**, 391–399 (2002).
  20. W. Ma, N. Vigneron, J. Chapiro, V. Stroobant, C. Germeau, T. Boon, P. G. Coulie, B. J. Van Den Eynde, A MAGE-C2 antigenic peptide processed by the immunoproteasome is recognized by cytolytic T cells isolated from a melanoma patient after successful immunotherapy. *Int. J. Cancer*. **129**, 2427–2434 (2011).
  21. N. Vigneron, J. Abi Habib, B. J. Van den Eynde, Learning from the Proteasome: How To Fine-Tune Cancer Immunotherapy. *Trends in Cancer*. **3** (2017), pp. 726–741.
  22. J. Neefjes, H. Ovaa, A peptide’s perspective on antigen presentation to the immune system. *Nat. Chem. Biol.* **9** (2013), pp. 769–775.
  23. K. Woods, A. J. Knights, M. Anaka, R. B. Schittenhelm, A. W. Purcell, A. Behren, J. Cebon, Mismatch in epitope specificities between IFN $\gamma$  inflamed and uninfamed conditions leads to escape from T lymphocyte

killing in melanoma. *J. Immunother. Cancer*. **4**, 10 (2016).

24. U. Salzmann, S. Kral, B. Braun, S. Standera, M. Schmidt, P.-M. Klotzel, A. Sijts, Mutational analysis of subunit  $\beta 2$  (MECL-1) demonstrates conservation of cleavage specificity between yeast and mammalian proteasomes. *FEBS Lett.* **454**, 11–15 (1999).
25. J. Driscoll, M. G. Brown, D. Finley, J. J. Monaco, MHC-linked LMP gene products specifically alter peptidase activities of the proteasome. *Nature*. **365**, 262–264 (1993).
26. M. Gaczynska, K. L. Rock, A. L. Goldberg,  $\gamma$ -Interferon and expression of MHC genes regulate peptide hydrolysis by proteasomes. , *Publ. online 16 Sept. 1993*; / doi10.1038/365264a0. **365**, 264 (1993).
27. D. A. Ferrington, D. S. Gregerson, Immunoproteasomes: structure, function, and antigen presentation. *Prog. Mol. Biol. Transl. Sci.* **109**, 75–112 (2012).
28. I. E. Kammerl, S. Meiners, Proteasome function shapes innate and adaptive immune responses. *Am. J. Physiol. - Lung Cell. Mol. Physiol.* **311** (2016).
29. G. A. Collins, A. L. Goldberg, The Logic of the 26S Proteasome. *Cell*. **169**, 792–806 (2017).
30. O. Cux, B. A. Zieba, S. Meiners, in *Advances in Experimental Medicine and Biology* (Springer, 2020), vol. 1233, pp. 55–100.
31. A. Rousseau, A. Bertolotti, Regulation of proteasome assembly and activity in health and disease. *Nat. Rev. Mol. Cell Biol.* **19**, 697–712 (2018).
32. A. Rodriguez, A. Perez-Gonzalez, A. Nieto, Influenza Virus Infection Causes Specific Degradation of the Largest Subunit of Cellular RNA Polymerase II. *J. Virol.* **81**, 5315–5324 (2007).
33. I. K. Mandemaker, M. E. Geijer, I. Kik, K. Bezstarosti, E. Rijkers, A. Raams, R. C. Janssens, H. Lans, J. H. Hoeijmakers, J. A. Demmers, W. Vermeulen, J. A. Marteijn, DNA damage-induced replication stress results in PA200-proteasome-mediated degradation of acetylated histones. *EMBO Rep.* **19** (2018), doi:10.15252/embr.201745566.
34. B. Khor, A. L. Bredemeyer, C.-Y. Huang, I. R. Turnbull, R. Evans, L. B. Maggi, J. M. White, L. M. Walker, K. Carnes, R. A. Hess, B. P. Sleckman, Proteasome activator PA200 is required for normal spermatogenesis. *Mol. Cell. Biol.* **26**, 2999–3007 (2006).
35. J. Blickwedehl, S. Olejniczak, R. Cummings, N. Sarvaiya, A. Mantilla, A. Chanan-Khan, T. K. Pandita, M. Schmidt, C. B. Thompson, N. Bangia, The proteasome activator PA200 regulates tumor cell responsiveness to glutamine and resistance to ionizing radiation. *Mol. Cancer Res.* **10**, 937–944 (2012).
36. V. Ustrell, L. Hoffman, G. Pratt, M. Rechsteiner, Pa200, a nuclear proteasome activator involved in DNA repair. *EMBO J.* **21**, 3516–3525 (2002).
37. V. Welk, O. Cux, V. Kleene, C. Abeza, D. Trumbach, O. Eickelberg, S. Meiners, Inhibition of proteasome activity induces formation of alternative proteasome complexes. *J. Biol. Chem.* **291**, 13147–13159 (2016).
38. M.-X. Qian, Y. Pang, C. H. Liu, K. Haratake, B.-Y. Du, D.-Y. Ji, G.-F. Wang, Q.-Q. Zhu, W. Song, Y. Yu, X.-X. Zhang, H.-T. Huang, S. Miao, L.-B. Chen, Z.-H. Zhang, Y.-N. Liang, S. Liu, H. Cha, D. Yang, Y. Zhai, T. Komatsu, F. Tsuruta, H. Li, C. Cao, W. Li, G.-H. Li, Y. Cheng, T. Chiba, L. Wang, A. L. Goldberg, Y. Shen, X.-B. Qiu, Acetylation-Mediated Proteasomal Degradation of Core Histones during DNA Repair and Spermatogenesis. *Cell*. **153**, 1012–1024 (2013).
39. I. K. Mandemaker, M. E. Geijer, I. Kik, K. Bezstarosti, E. Rijkers, A. Raams, R. C. Janssens, H. Lans, J. H. Hoeijmakers, J. A. Demmers, W. Vermeulen, J. A. Marteijn, DNA damage-induced replication stress

results in PA200-proteasome-mediated degradation of acetylated histones. *EMBO Rep.* **19**, e45566 (2018).

40. A. N. Antoniou, I. Lenart, D. B. Guiliano, S. J. Powis, in *Vaccinology: Principles and Practice* (Wiley-Blackwell, Department of Infection and Immunity/Centre for Rheumatology, University College London, London, United Kingdom, 2012), pp. 29–46.
41. B. Fabre, T. Lambour, L. Garrigues, M. Ducoux-Petit, F. Amalric, B. Monsarrat, O. Burlet-Schiltz, M. P. Bousquet-Dubouch, Label-free quantitative proteomics reveals the dynamics of proteasome complexes composition and stoichiometry in a wide range of human cell lines. *J. Proteome Res.* **13**, 3027–3037 (2014).
42. B. Fabre, T. Lambour, L. Garrigues, F. Amalric, N. Vigneron, T. Menneteau, A. Stella, B. Monsarrat, B. Van den Eynde, O. Burlet-Schiltz, M. Bousquet-Dubouch, Deciphering preferential interactions within supramolecular protein complexes: the proteasome case. *Mol. Syst. Biol.* **11**, 771 (2015).
43. A. V. Morozov, V. L. Karpov, *Proteasomes and several aspects of their heterogeneity relevant to cancer* (Frontiers Media S.A., 2019), vol. 9.
44. M. Raule, F. Cerruti, N. Benaroudj, R. Migotti, J. Kikuchi, A. Bachi, A. Navon, G. Dittmar, P. Cascio, PA28 $\alpha\beta$  Reduces Size and Increases Hydrophilicity of 20S Immunoproteasome Peptide Products. *Chem. Biol.* **21**, 470–480 (2014).
45. A. Toste Rêgo, P. C. A. da Fonseca, Characterization of Fully Recombinant Human 20S and 20S-PA200 Proteasome Complexes. *Mol. Cell.* **76**, 138-147.e5 (2019).
46. H. Wolf-Levy, A. Javitt, A. Eisenberg-Lerner, A. Kacen, A. Ulman, D. Sheban, B. Dassa, V. Fishbain-Yoskovitz, C. Carmona-Rivera, M. P. Kramer, N. Nudel, I. Regev, L. Zahavi, D. Elinger, M. J. Kaplan, D. Morgenstern, Y. Levin, Y. Merbl, Revealing the cellular degradome by mass spectrometry analysis of proteasome-cleaved peptides. *Nat. Biotechnol.* **36**, 1110–1116 (2018).
47. A. Javitt, Y. Merbl, Global views of proteasome-mediated degradation by mass spectrometry. *Expert Rev. Proteomics*, 1–6 (2019).
48. E. A. Collisson, J. D. Campbell, A. N. Brooks, A. H. Berger, W. Lee, J. Chmielecki, D. G. Beer, L. Cope, C. J. Creighton, L. Danilova, L. Ding, G. Getz, P. S. Hammerman, D. N. Hayes, B. Hernandez, J. G. Herman, J. V. Heymach, I. Jurisica, R. Kucherlapati, D. Kwiatkowski, M. Ladanyi, G. Robertson, N. Schultz, R. Shen, R. Sinha, C. Sougnez, M. S. Tsao, W. D. Travis, J. N. Weinstein, D. A. Wigle, M. D. Wilkerson, A. Chu, A. D. Cherniack, A. Hadjipanayis, M. Rosenberg, D. J. Weisenberger, P. W. Laird, A. Radenbaugh, S. Ma, J. M. Stuart, L. A. Byers, S. B. Baylin, R. Govindan, M. Meyerson, S. B. Gabriel, K. Cibulskis, J. Kim, C. Stewart, L. Lichtenstein, E. S. Lander, M. S. Lawrence, E. Getz, R. Fulton, L. L. Fulton, M. D. McLellan, R. K. Wilson, K. Ye, C. C. Fronick, C. A. Maher, C. A. Miller, M. C. Wendl, C. Cabanski, E. Mardis, D. Wheeler, M. Balasundaram, Y. S. N. Butterfield, R. Carlsen, E. Chuah, N. Dhalla, R. Guin, C. Hirst, D. Lee, H. I. Li, M. Mayo, R. A. Moore, A. J. Mungall, J. E. Schein, P. Sipahimalani, A. Tam, R. Varhol, A. G. Robertson, N. Wye, N. Thiessen, R. A. Holt, S. J. M. Jones, M. A. Marra, M. Imielinski, R. C. Onofrio, E. Hodis, T. Zack, E. Helman, C. S. Pedamallu, J. Mesirov, G. Saksena, S. E. Schumacher, S. L. Carter, L. Garraway, R. Beroukhim, S. Lee, H. S. Mahadeshwar, A. Pantazi, A. Protopopov, X. Ren, S. Seth, X. Song, J. Tang, L. Yang, J. Zhang, P. C. Chen, M. Parfenov, A. W. Xu, N. Santoso, L. Chin, P. J. Park, K. A. Hoadley, J. T. Auman, S. Meng, Y. Shi, E. Buda, S. Waring, U. Veluvolu, D. Tan, P. A. Mieczkowski, C. D. Jones, J. V. Simons, M. G. Soloway, T. Bodenheimer, S. R. Jefferys, J. Roach, A. P. Hoyle, J. Wu, S. Balu, D. Singh, J. F. Prins, J. S. Marron, J. S. Parker, C. M. Perou, J. Liu, D. T. Maglinte, P. H. Lai, M. S. Bootwalla, D. J. Van Den Berg, T. Triche, J. Cho, D. DiCara, D. Heiman, P. Lin, W. Mallard, D. Voet, H. Zhang, L. Zou, M. S. Noble, N. Gehlenborg, H. Thorvaldsdottir, M. D. Nazaire, J. Robinson, B. A. Aksoy, G. Ciriello, B. S. Taylor, G. Dresdner, J. Gao, B. Gross, V. E. Seshan, B. Reva, S. O. Sumer, N. Weinhold, C. Sander, S. Ng, J. Zhu, C. C. Benz, C. Yau,

- D. Haussler, P. T. Spellman, P. K. Kimes, B. M. Broom, J. Wang, Y. Lu, P. K. S. Ng, L. Diao, W. Liu, C. I. Amos, R. Akbani, G. B. Mills, E. Curley, J. Paulauskis, K. Lau, S. Morris, T. Shelton, D. Mallery, J. Gardner, R. Penny, C. Saller, K. Tarvin, W. G. Richards, R. Cerfolio, A. Bryant, D. P. Raymond, N. A. Pennell, C. Farver, C. Czerwinski, L. Huelsenbeck-Dill, M. Iacocca, N. Petrelli, B. Rabeno, J. Brown, T. Bauer, C. O. Dolzhanskiy, O. Potapova, D. Rotin, O. Voronina, E. Nemirovich-Danchenko, K. V. Fedosenko, A. Gal, M. Behera, S. S. Ramalingam, G. Sica, D. Flieder, J. Boyd, J. E. Weaver, B. Kohl, D. H. Q. Thinh, G. Sandusky, H. Juhl, E. Duhig, P. Illei, E. Gabrielson, J. Shin, B. Lee, K. Rogers, D. Trusty, M. V. Brock, C. Williamson, E. Burks, K. Rieger-Christ, A. Holway, T. Sullivan, M. K. Asiedu, F. Kosari, N. Rekhtman, M. Zakowski, V. W. Rusch, P. Zippile, J. Suh, H. Pass, C. Goparaju, Y. Owusu-Sarpong, J. M. S. Bartlett, S. Kodeeswaran, J. Parfitt, H. Sekhon, M. Albert, J. Eckman, J. B. Myers, C. Morrison, C. Gaudio, J. A. Borgia, P. Bonomi, M. Pool, M. J. Liptay, F. Moiseenko, I. Zaytseva, H. Dienemann, M. Meister, P. A. Schnabel, T. R. Muley, M. Peifer, C. Gomez-Fernandez, L. Herbert, S. Egea, M. Huang, L. B. Thorne, L. Boice, A. H. Salazar, W. K. Funkhouser, W. K. Rathmell, R. Dhir, S. A. Yousem, S. Dacic, F. Schneider, J. M. Siegfried, R. Hajek, M. A. Watson, S. McDonald, B. Meyers, B. Clarke, I. A. Yang, K. M. Fong, L. Hunter, M. Windsor, R. V. Bowman, S. Peters, I. Letovanec, K. Z. Khan, M. A. Jensen, E. E. Snyder, D. Srinivasan, A. B. Kahn, J. Baboud, D. A. Pot, K. R. M. Shaw, M. Sheth, T. Davidsen, J. A. Demchok, L. Yang, Z. Wang, R. Tarnuzzer, J. C. Zenklusen, B. A. Ozenberger, H. J. Sofia, R. Cheney, Comprehensive molecular profiling of lung adenocarcinoma: The cancer genome atlas research network. *Nature*. **511**, 543–550 (2014).
49. M. Boulpicate, R. Darrigrand, A. Pierson, V. Salgues, M. Rouillon, B. Gaudineau, M. Khaled, A. Cattaneo, A. Bachi, P. Cascio, S. Apcher, Tumors escape immunosurveillance by overexpressing the proteasome activator PSME3. *Oncoimmunology*. **9**, 1761205 (2020).
  50. S. Xiong, Y. Zheng, P. Jiang, R. Liu, X. Liu, J. Qian, J. Gu, L. Chang, D. Ge, Y. Chu, PA28gamma emerges as a novel functional target of tumour suppressor microRNA-7 in non-small-cell lung cancer. *Br. J. Cancer*. **110**, 353–362 (2014).
  51. I. E. Kammerl, A. Caniard, J. Merl-Pham, G. Ben-Nissan, C. H. Mayr, A. Mossina, A. Geerlof, O. Eickelberg, S. M. Hauck, M. Sharon, S. Meiners, Dissecting the molecular effects of cigarette smoke on proteasome function. *J. Proteomics*. **193**, 1–9 (2019).
  52. Huating Yuan, Min Yan, Guanxiong Zhang, Wei Liu, Chunyu Deng, Gaoming Liao, Liwen Xu, Tao Luo, Haoteng Yan, Zhilin Long, Aiai Shi, Tingting Zhao, Yun Xiao, Xia Li, CancerSEA: A Cancer Single-Cell State Atlas - PubMed. *Nucleic Acids Res.* (2019).
  53. M. B. Winter, F. La Greca, S. Arastu-Kapur, F. Caiazza, P. Cimerancic, T. J. Buchholz, J. L. Anderl, M. Ravalin, M. F. Bohn, A. Sali, A. J. O'Donoghue, C. S. Craik, Immunoproteasome functions explained by divergence in cleavage specificity and regulation. *Elife*. **6**, e27364 (2017).
  54. A. F. Kisselev, A. L. Goldberg, Monitoring activity and inhibition of 26S proteasomes with fluorogenic peptide substrates. *Methods Enzymol.* **398** (2005), pp. 364–378.
  55. C. Chong, F. Marino, H. Pak, J. Racle, R. T. Daniel, M. Müller, D. Gfeller, G. Coukos, M. Bassani-Sternberg, High-throughput and Sensitive Immunopeptidomics Platform Reveals Profound Interferon-Mediated Remodeling of the Human Leukocyte Antigen (HLA) Ligandome. *Mol. Cell. Proteomics*. **17**, 533–548 (2018).
  56. A. Javitt, E. Barnea, M. P. Kramer, H. Wolf-Levy, Y. Levin, A. Admon, Y. Merbl, Pro-inflammatory cytokines alter the immunopeptidome landscape by modulation of HLA-B expression. *Front. Immunol.* **10**, 141 (2019).
  57. L. Avallé, S. Pensa, G. Regis, F. Novelli, V. Poli, STAT1 and STAT3 in tumorigenesis. *JAK-STAT*. **1**, 65–72 (2012).



58. C. Chong, F. Marino, H. Pak, J. Racle, R. T. Daniel, M. Müller, D. Gfeller, G. Coukos, M. Bassani-Sternberg, High-throughput and Sensitive Immunopectidomics Platform Reveals Profound Interferony-Mediated Remodeling of the Human Leukocyte Antigen (HLA) Ligandome. *Mol. Cell. Proteomics*. **17**, 533–548 (2018).
59. L. Komov, D. M. Kadosh, E. Barnea, E. Milner, A. Hendler, A. Admon, Cell Surface MHC Class I Expression Is Limited by the Availability of Peptide-Receptive “Empty” Molecules Rather than by the Supply of Peptide Ligands. *Proteomics*. **18**, 1700248 (2018).
60. N. Riaz, J. J. Havel, V. Makarov, A. Desrichard, W. J. Urba, J. S. Sims, F. S. Hodi, S. Martín-Algarra, R. Mandal, W. H. Sharfman, S. Bhatia, W.-J. Hwu, T. F. Gajewski, C. L. Slingluff, D. Chowell, S. M. Kendall, H. Chang, R. Shah, F. Kuo, L. G. T. Morris, J.-W. Sidhom, J. P. Schneck, C. E. Horak, N. Weinhold, T. A. Chan, Tumor and Microenvironment Evolution during Immunotherapy with Nivolumab. *Cell*. **171**, 934-949.e16 (2017).
61. P. A. Ott, Z. Hu, D. B. Keskin, S. A. Shukla, J. Sun, D. J. Bozym, W. Zhang, A. Luoma, A. Giobbie-Hurder, L. Peter, C. Chen, O. Olive, T. A. Carter, S. Li, D. J. Lieb, T. Eisenhaure, E. Gjini, J. Stevens, W. J. Lane, I. Javeri, K. Nellaippan, A. M. Salazar, H. Daley, M. Seaman, E. I. Buchbinder, C. H. Yoon, M. Harden, N. Lennon, S. Gabriel, S. J. Rodig, D. H. Barouch, J. C. Aster, G. Getz, K. Wucherpfennig, D. Neuberg, J. Ritz, E. S. Lander, E. F. Fritsch, N. Hacohen, C. J. Wu, An immunogenic personal neoantigen vaccine for patients with melanoma. *Nature*. **547**, 217–221 (2017).
62. U. Sahin, Ö. Türeci, Personalized vaccines for cancer immunotherapy. *Science* (80-. ). **359**, 1355–1360 (2018).
63. Y. Chu, Q. Liu, J. Wei, B. Liu, Personalized cancer neoantigen vaccines come of age. *Theranostics*. **8**, 4238–4246 (2018).
64. T. N. Schumacher, W. Scheper, P. Kvistborg, Cancer Neoantigens. *Annu. Rev. Immunol.* **37**, 173–200 (2019).
65. A. M. Cantin, M. V. Richter, Cigarette Smoke-Induced Proteostasis Imbalance in Obstructive Lung Diseases. *Curr. Mol. Med.* **12**, 836–849 (2012).
66. U. S. Srinivas, B. W. Q. Tan, B. A. Vellayappan, A. D. Jeyasekharan, ROS and the DNA damage response in cancer. *Redox Biol.* **25** (2019), p. 101084.
67. A. M. Ahmed, in *Oxidative Stress in Lung Diseases* (Springer Singapore, 2019), pp. 99–113.
68. V. Welk, T. Meul, C. Lukas, I. E. Kammerl, S. R. Mulay, A. C. Schamberger, N. Semren, I. E. Fernandez, H. J. Anders, A. Günther, J. Behr, O. Eickelberg, M. Korfei, S. Meiners, Proteasome activator PA200 regulates myofibroblast differentiation. *Sci. Rep.* **9**, 1–11 (2019).
69. J. A. Trujillo, R. F. Sweis, R. Bao, J. J. Luke, T cell–inflamed versus Non-T cell–inflamed tumors: a conceptual framework for cancer immunotherapy drug development and combination therapy selection. *Cancer Immunol. Res.* **6**, 990–1000 (2018).
70. S. Spranger, R. Bao, T. F. Gajewski, Melanoma-intrinsic  $\beta$ -catenin signalling prevents anti-tumour immunity. *Nature*. **523**, 231–235 (2015).
71. Zuguang Gu, Roland Eils, Matthias Schlesner, Complex Heatmaps Reveal Patterns and Correlations in Multidimensional Genomic Data - PubMed. *Bioinformatics* (2016), doi:10.1093/bioinformatics/btw313.
72. H. Wickam, *ggplot2: Elegant Graphics for Data Analysis* (Springer-Verlag New York, 2016).
73. M. Uhlen, C. Zhang, S. Lee, E. Sjöstedt, L. Fagerberg, G. Bidkhori, R. Benfeitas, M. Arif, Z. Liu, F.

Edfors, K. Sanli, K. Von Feilitzen, P. Oksvold, E. Lundberg, S. Hober, P. Nilsson, J. Mattsson, J. M. Schwenk, H. Brunnström, B. Glimelius, T. Sjöblom, P. H. Edqvist, D. Djureinovic, P. Micke, C. Lindskog, A. Mardinoglu, F. Ponten, A pathology atlas of the human cancer transcriptome. *Science* (80-. ). **357** (2017), doi:10.1126/science.aan2507.

74. P. J. Thul, L. Akesson, M. Wiking, D. Mahdessian, A. Geladaki, H. Ait Blal, T. Alm, A. Asplund, L. Björk, L. M. Breckels, A. Bäckström, F. Danielsson, L. Fagerberg, J. Fall, L. Gatto, C. Gnann, S. Hober, M. Hjelmare, F. Johansson, S. Lee, C. Lindskog, J. Mulder, C. M. Mulvey, P. Nilsson, P. Oksvold, J. Rockberg, R. Schutten, J. M. Schwenk, A. Sivertsson, E. Sjöstedt, M. Skogs, C. Stadler, D. P. Sullivan, H. Tegel, C. Winsnes, C. Zhang, M. Zwahlen, A. Mardinoglu, F. Pontén, K. Von Feilitzen, K. S. Lilley, M. Uhlén, E. Lundberg, A subcellular map of the human proteome. *Science* (80-. ). **356** (2017), doi:10.1126/science.aal3321.
75. M. Uhlén, L. Fagerberg, B. M. Hallström, C. Lindskog, P. Oksvold, A. Mardinoglu, Å. Sivertsson, C. Kampf, E. Sjöstedt, A. Asplund, I. M. Olsson, K. Edlund, E. Lundberg, S. Navani, C. A. K. Szigartyo, J. Odeberg, D. Djureinovic, J. O. Takanen, S. Hober, T. Alm, P. H. Edqvist, H. Berling, H. Tegel, J. Mulder, J. Rockberg, P. Nilsson, J. M. Schwenk, M. Hamsten, K. Von Feilitzen, M. Forsberg, L. Persson, F. Johansson, M. Zwahlen, G. Von Heijne, J. Nielsen, F. Pontén, Tissue-based map of the human proteome. *Science* (80-. ). **347** (2015), doi:10.1126/science.1260419.
76. Iris Kamer , Elizabeta Bab-Dinitz , Oranit Zadok , Efrat Ofek , Teodor Gottfried , Inbal Daniel-Meshulam , Goni Hout-Siloni , Alon Ben Nun, Iris Barshack, Amir Onn, Jair Bar, Immunotherapy response modeling by ex-vivo organ culture for lung cancer. *in Review*
77. J. A. Vizcaíno, A. Csordas, N. del-Toro, J. A. Dianes, J. Griss, I. Lavidas, G. Mayer, Y. Perez-Riverol, F. Reisinger, T. Ternent, Q.-W. Xu, R. Wang, H. Hermjakob, 2016 update of the PRIDE database and its related tools. *Nucleic Acids Res.* **44**, D447–D456 (2016).